

Tracking chromatin state changes using nanoscale photo-proximity labelling

<https://doi.org/10.1038/s41586-023-05914-y>

Received: 20 January 2022

Accepted: 2 March 2023

Published online: 05 April 2023



Ciaran P. Seath^{1,2,3,5}, Antony J. Burton^{2,4,5}, Xuemeng Sun², Gihoon Lee², Ralph E. Kleiner², David W. C. MacMillan^{1,2}✉ & Tom W. Muir²✉

Interactions between biomolecules underlie all cellular processes and ultimately control cell fate. Perturbation of native interactions through mutation, changes in expression levels or external stimuli leads to altered cellular physiology and can result in either disease or therapeutic effects^{1,2}. Mapping these interactions and determining how they respond to stimulus is the genesis of many drug development efforts, leading to new therapeutic targets and improvements in human health¹. However, in the complex environment of the nucleus, it is challenging to determine protein–protein interactions owing to low abundance, transient or multivalent binding and a lack of technologies that are able to interrogate these interactions without disrupting the protein-binding surface under study³. Here, we describe a method for the traceless incorporation of iridium-photosensitizers into the nuclear micro-environment using engineered split inteins. These Ir-catalysts can activate diazirine warheads through Dexter energy transfer to form reactive carbenes within an approximately 10 nm radius, cross-linking with proteins in the immediate micro-environment (a process termed μ Map) for analysis using quantitative chemoproteomics⁴. We show that this nanoscale proximity-labelling method can reveal the critical changes in interactomes in the presence of cancer-associated mutations, as well as treatment with small-molecule inhibitors. μ Map improves our fundamental understanding of nuclear protein–protein interactions and, in doing so, is expected to have a significant effect on the field of epigenetic drug discovery in both academia and industry.

Mapping protein–protein interactions (PPIs) is central to our understanding of cellular biology⁵. The enormous challenges associated with this undertaking are magnified in the nucleus in which transient and multivalent interactions, fine-tuned by posttranslational modifications (PTMs), combine to choreograph DNA-templated processes such as transcription⁶. Perturbations to these regulatory mechanisms often lead to disease⁷, for example, somatic mutations that alter the composition and activity of chromatin-associated protein complexes are implicated in many human cancers and developmental disorders^{8–10}. Moreover, recent studies have shown that histone proteins are themselves frequently mutated in cancers^{11–13}. Understanding how these mutations lead to, or perpetuate, disease is the focus of intense investigation^{11–13}, work that necessitates accurate comparative mapping of chromatin-associated PPI networks as a function of altered cell states¹.

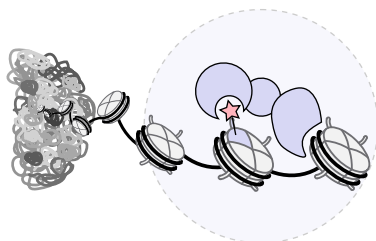
The elucidation of nuclear PPIs has typically been performed by immunoprecipitation–mass spectrometry (IP–MS) workflows, in which antibodies recognizing selected proteins are used to enrich their target along with direct interactors¹⁴. However, IP–MS approaches rely on nuclear lysates as input, which may not be ideal for every system^{15,16}, especially when the interactions are transient in nature (for

example, driven by posttranslational modification) or require multi-protein complexes that bridge native chromatin^{17–19}. This has fuelled the development of chemoproteomics approaches such as those based on photocrosslinking^{20,21} or proximity-labelling^{22–24} technologies that seek to capture PPIs in a native-like environment. Despite these ongoing advances, no single method exists to map chromatin interactomes in a general and unbiased manner and particularly to discern how such interactions are affected by perturbations such as mutation or drug treatment (Fig. 1a). To address this need we considered the union of technologies recently disclosed by our two laboratories, μ Map⁴ and in nucleosome protein *trans*-splicing²⁰, to enable a traceless, short-range proximity-labelling method that can be readily deployed to any nuclear protein target. Protein *trans*-splicing using ultrafast split inteins facilitates the installation of iridium (Ir)-photocatalysts onto the N or C termini of target proteins. On irradiation with blue light-emitting diodes (LEDs) in the presence of a biotin–diazirine probe, localized carbene generation (through Dexter energy transfer from photo-excited iridium to aryl diazirines) allows interactomes to be determined, specifically those within about 10 nm of the iridium-centred photocatalyst (Fig. 1b).

¹Merck Center for Catalysis at Princeton University, Princeton, NJ, USA. ²Department of Chemistry, Princeton University, Princeton, NJ, USA. ³Present address: Department of Chemistry, Scripps-UF, Jupiter, FL, USA. ⁴Present address: Discovery Biology, Discovery Sciences, Biopharmaceuticals R&D, AstraZeneca, Waltham, MA, USA. ⁵These authors contributed equally: Ciaran P. Seath, Antony J. Burton. ✉e-mail: dmacmill@princeton.edu; muir@princeton.edu

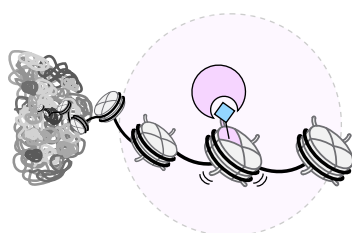
a Perturbations at chromatin lead to changes in interactome and phenotype

Chromatin interactomes



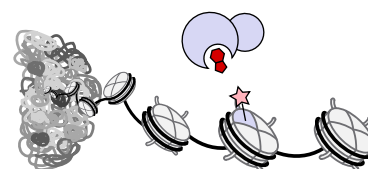
- Critical for transcriptional regulation
- Modulated by posttranslational modification

Oncomutation interactomes



- Perturbed chromatin interactomes
- Affect chromatin remodelling and transcription
- Promote proliferation and cancer progression

Epigenetic drug on/off targets



- Block chromatin PPIs
- Critical therapeutic strategies
- Target histone writers, readers, erasers and chromatin remodellers

Can μ Map reveal the mechanisms behind how chromatin perturbations lead to disease or therapy?

b μ Map photocatalytic proximity labelling captures close-range interactions on nuclear proteins

μ Map catalyst (Ir) incorporation via rapid intein *trans*-splicing

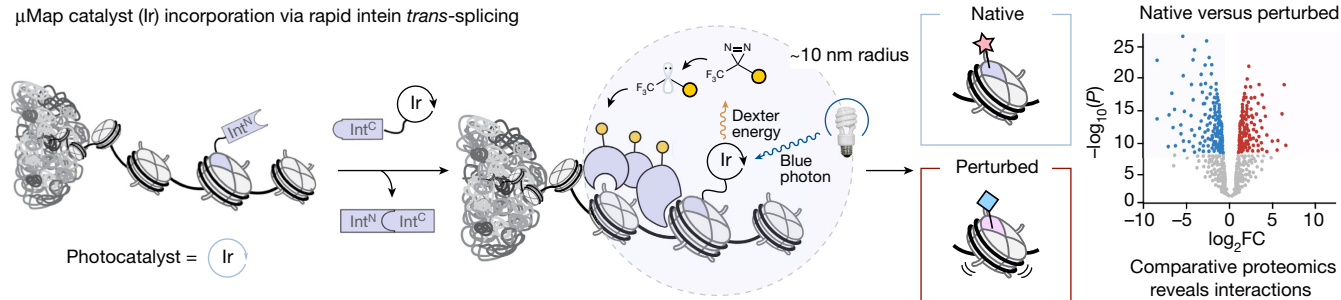


Fig. 1 | Development of a catalytic labelling platform using inteins.

a, Chromatin interactomes can be perturbed through mutation leading to oncogenic phenotypes. Epigenetic drugs alter the chromatin interactome for therapeutic benefit. **b**, Cartoon showing strategy for nuclear photo-proximity labelling. Ir-photocatalysts can be incorporated into nuclear proteins via protein *trans*-splicing. The N-terminal fragment of Cfa^N is fused to a target nuclear protein, whereas Cfa^C is linked to the photocatalyst. In nucleospllicing provides Ir-conjugated nuclear proteins. Following excitation under blue light

irradiation, the photocatalyst activates diazirines (to form carbenes via loss of molecular nitrogen) through a process called Dexter energy transfer. These carbenes are then poised to insert into neighbouring proteins that can be enriched using streptavidin beads. Comparative chemoproteomic analysis reveals how a given perturbation (for example, a mutation or drug treatment) affects local interactomes, providing insights into the mechanistic basis for disease or therapy. The mock volcano plot in Fig. 1 was created using BioRender.

Our proposed workflow offers distinct advantages for the elucidation of subtly perturbed chromatin interactomes through mutation or ligand binding. Principally, the short radius afforded by this technology limits labelling to the close vicinity of a designated chromatin factor or nucleosome, only identifying proteins that are affected by a particular mutation or pharmacological intervention. This is critically important, given the structural and functional heterogeneity of chromatin²⁵. Furthermore, the incorporation of the μ Map catalyst is designed to be almost traceless and its small size is expected to minimize disruption to the native environment (for example, in comparison to fusion proteins), allowing the study of modifications that only minimally change the native interactome.

We began our studies by preparing an Ir-conjugated intein fragment (complementary C-terminal fragment Cfa^C-Ir), using a combination of solid-phase peptide synthesis and click chemistry (Fig. 2a,b). We next fused the N-terminal fragment of the engineered Cfa split intein (Cfa^N)^{26,27} to the C terminus of histone H3.1. For analytical convenience, we also included HA and FLAG epitope tags flanking the intein (Fig. 2c). We then treated nuclei isolated from these transfected cells with the complementary split intein fragment (Cfa^C) linked to the Ir photocatalyst. This resulted in the site-selective incorporation of the photocatalyst onto the C terminus of H3.1 through in nucleospllicing (Fig. 2e). Irradiation of these nuclei in the presence of

the diazine-biotin probe (Fig. 2d) led to dramatically enhanced protein labelling compared to control reactions that excluded Cfa^C-Ir or diazine-biotin (Fig. 2f). Elution from streptavidin beads showed strong enrichment of histone H3 by western blot (Fig. 2f).

We established a tandem mass tag (TMT)-based quantitative chemoproteomics workflow to determine the interactome for H3.1 versus the centromere-specific H3 variant CENP-A (Fig. 2g,h and Extended Data Fig. 1) to assess whether our workflow could delineate between nucleosomal interactomes at specific regions of chromatin. We used cut-offs of more than 0.5 log fold change (log₂FC) and false discovery rate (FDR)-corrected $P < 0.05$ and hits were found in all replicates. Note, further analyses of the proteomic datasets in this study are provided in Extended Data Fig. 10. Comparison of the H3.1 versus CENP-A interactomes returned established H3.1-modifying enzymes (for example, EHMT2 and SUV39H1) and reader proteins (for example, HP1 isoforms) (Fig. 2b and Extended Data Fig. 10; see Supplementary Information for full data table)^{28,29}. CENP-A interacting proteins included both members of the FACT complex (SSRP1 and SPT16) involved in the deposition of CENP-A into chromatin (Fig. 2b)³⁰. Consistent with the centromeric localization of CENP-A, we see enrichment of transcriptional regulators (CBX6, DNMT3A, CHD4, RBBP4, KAT7 and KMT2A) only in the H3.1 samples. Furthermore, gene ontology (GO) analysis of the H3.1 hits showed strong enrichment of chromatin

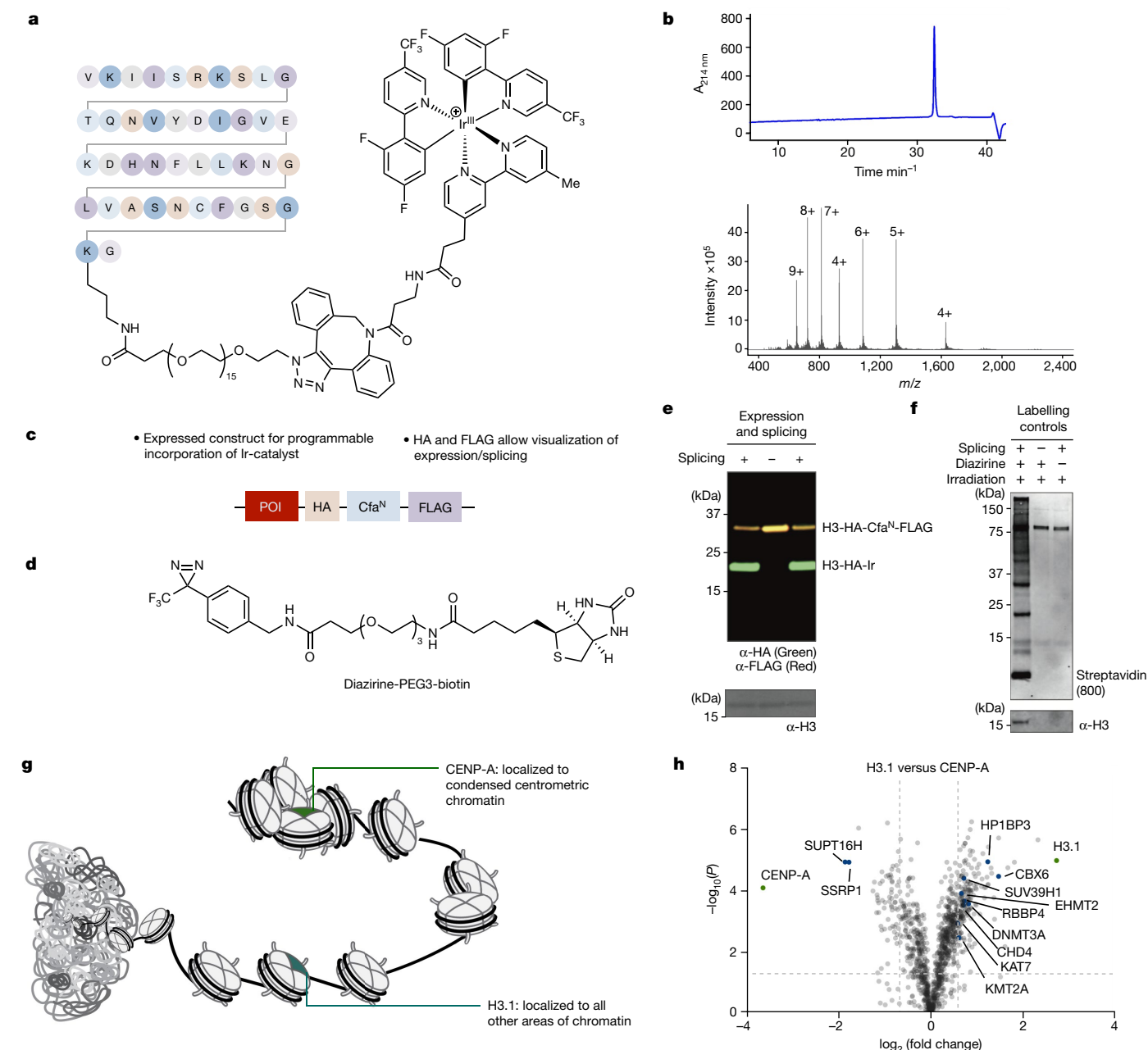


Fig. 2 | Development of a chromatin-localized μ Map proximity-labelling platform. **a**, Structure of the Cfa^C-Ir construct used in this study. **b**, High-performance liquid chromatography trace (top) and electrospray ionization MS spectrum (bottom) for purified Cfa^C-Ir (calculated $[M]^+ = 6,514.6$ Da; observed $[M]^+ = 6,514.1$ Da). **c**, General design of constructs used for μ Map. **d**, Structure of diazine-PEG3-biotin probe used in this study. **e**, Validation of the approach using histone H3. In nucleosome protein *trans*-splicing with 0.5 μ M Cfa^C-Ir for 1 h results in the generation of the H3 spliced product (green) as shown by western blotting. **f**, Biotinylation of nuclear proteins, as detected by

streptavidin blotting, is dependent on irradiation, Cfa^C-Ir and the diazine probe. H3 is enriched following labelling and streptavidin enrichment. **g**, Graphic representing differential localization between histone H3.1 and centromeric variant CENP-A. **h**, Volcano plot derived from a two-sided *t*-test showing proteins enriched in a comparative proteomics study between H3.1 and CENP-A using the μ Map workflow. Selected proteins are highlighted that are discussed in the text. Dotted lines indicate cut-offs used. FDR values were calculated using the Benjamini–Hochberg procedure, as described in the Methods. For blot source data, see Supplementary Fig. 1.

organization ($-\log_{10}P = 56$), histone lysine methylation ($-\log_{10}P = 11$) and epigenetic regulation of gene expression ($-\log_{10}P = 25$) (Extended Data Fig. 1), consistent with the known role of H3.1 as a platform for transcriptional regulation.

With the basic chemoproteomics workflow established we questioned whether our method would sense subtle changes in nucleosomal structure, such as somatic mutations. Recent sequencing of patient tumour samples identified more than 4,000 histone mutations associated with a wide range of cancers^{11–13,31}. Determining whether

such mutations drive oncogenesis and cancer progression or are simply passenger mutations is critical to identifying new opportunities for therapeutic intervention. We sought to apply our method to the cancer-associated histone mutation H2A E92K, which is correlated with a range of cancers¹³. This mutation introduces a charge swap in the critical acidic patch interaction motif on the nucleosome, into which arginine residues of interacting proteins are known to anchor^{32–35}. We hoped that our methodology could shed light on to what extent chromatin PPLs are perturbed by this oncohistone mutation.

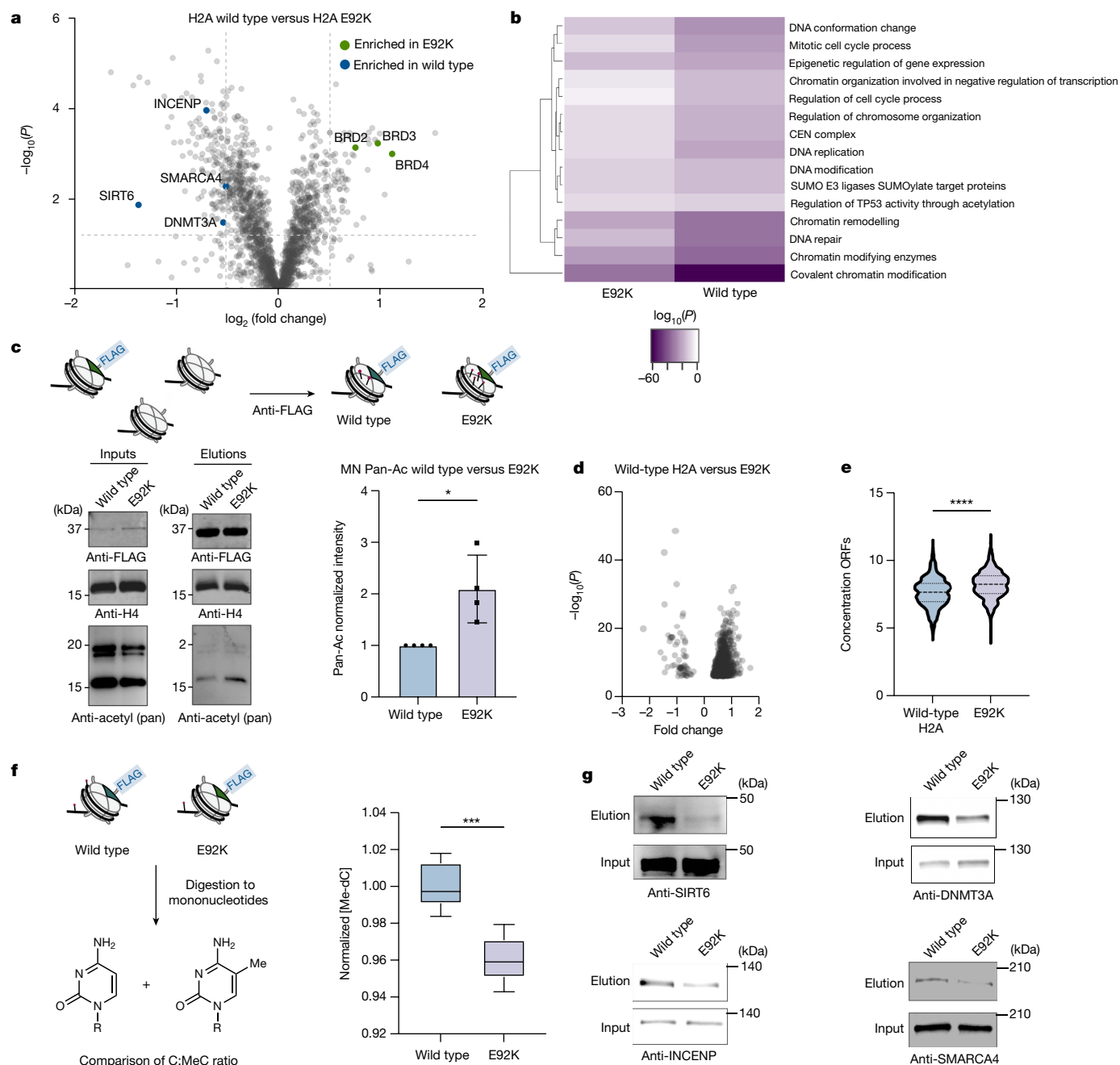


Fig. 3 | μ Map as a method to uncover oncogenic function of the somatic mutation H2A E92K. **a**, A volcano plot derived from a two-sided t -test showing protein interactors from the μ Map method comparing H2A to H2A E92K. Select proteins are highlighted. Dotted lines indicate cut-offs used. FDR values were calculated using the Benjamini–Hochberg procedure, as described in the Methods. **b**, Comparative GO analysis for wild-type versus E92K hits. GO terms consistent with the role of the acidic patch are de-enriched in the E92K mutant. **c**, Increased local acetylation of histone H4 is observed in the presence of H2A E92K, as determined by mononucleosome immunoprecipitation experiments. Western blot analysis showed an increase (2.1 ± 0.33) in acetylation in the E92K mutant compared to wild type. Bar plot shows change in acetylation levels on H4 normalized to wild type as determined by densitometry analysis of western blots (mean with s.d., $n = 4$ independent biological replicates, $P = 0.0156$). MN Pan-Ac, mononucleosome pan-acetylation levels. **d**, Volcano plot showing the concentration of significant (two-sided t -test, $P < 0.05$) ORFs in a comparative

ATAC-seq experiment between HEK 293T cells stably expressing wild-type H2A versus H2A E92K. **e**, Violin plot comparing the overall concentration of ORFs between HEK 293T cells stably expressing wild-type H2A versus H2A E92K from ATAC-seq analysis ($P = < 0.0001$, two-sided t -test). The data show that the E92K population has an increased concentration of ORFs when compared to the wild-type sample. **f**, Left, graphic showing experimental design for measuring local DNA methylation. Right, box-and-whisker plots showing local concentration of 5-methyl deoxycytosine (Me-dC) normalized to global Me-dC levels. E92K mutant shows a 5% decrease in methylation ($n = 6$ independent biological replicates, whiskers represent minimum to maximum, $P = 0.0003$, two-sided t -test). **g**, Western blot analysis comparing binding of selected proteins with either biotinylated wild-type nucleosomes or with biotinylated nucleosomes containing the H2A mutation E92K. * $P < 0.05$, *** $P < 0.001$, **** $P < 0.0001$. For blot source data, see Supplementary Fig. 1.

We found that the local chromatin micro-environment is indeed sensitive to the H2A E92K mutation (Fig. 3a and Extended Data Fig. 1; see Supplementary Information for full data table). GO analysis revealed

diminished enrichment of proteins related to chromatin modification and re-organization as a function of the perturbed acidic patch (Fig. 3b). Comparison of the dataset to the interactome of a construct

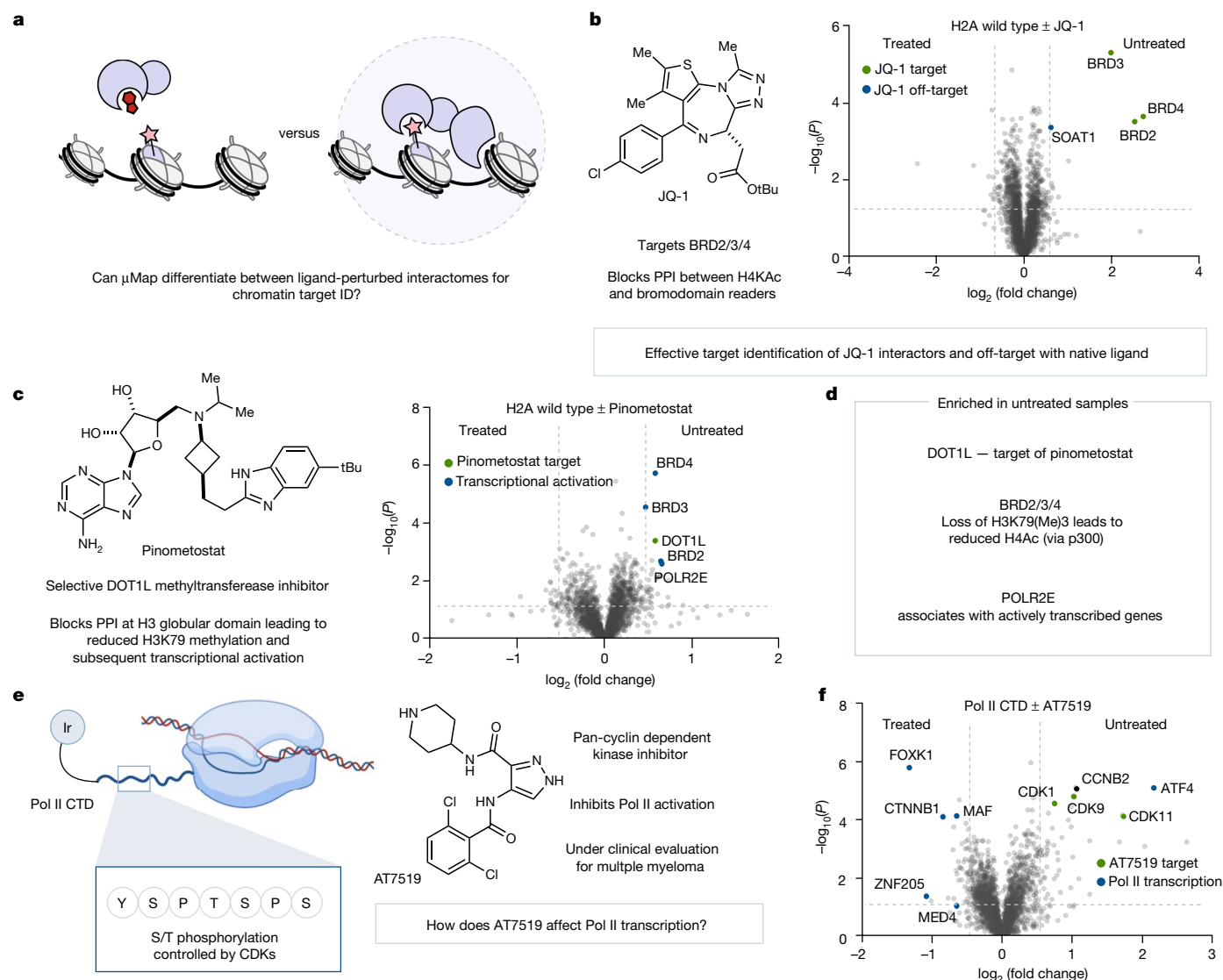


Fig. 4 | Interactome mapping of nuclear proteins to assess ligand interactions.

a, Performing the μ Map workflow in the presence of a bioactive ligand unveils PPIs that are disrupted or promoted by ligand treatment. This method can provide nuclear target identification data. **b**, Volcano plot derived from a two-sided t -test showing the H2A interactome versus H2A + 5 μ M JQ-1 (structure shown at left). This method identifies BRD2/3/4 as JQ-1 target proteins in addition to known off-target SOAT1. **c**, Volcano plot derived from a two-sided t -test showing the H2A interactome versus H2A + 2.5 μ M pinometostat.

Pinometostat target DOT1L is enriched in untreated cells, in addition to several proteins associated with loss of H3K79me. **d**, Summary of enriched proteins and their biological relevance is shown. **e**, RNA Pol II transcription is controlled by phosphorylation of the CTD. AT7519 inhibits CTD phosphorylation, stalling transcription. **f**, Volcano plot derived from a two-sided t -test showing RPBI-Ir versus RPBI-Ir + 2 μ M AT7519. Dotted lines indicate cut-offs used. FDR values were calculated using the Benjamini–Hochberg procedure, as described in the Methods.

with a triply mutated acidic patch (E61A, E90A and E92A) suggests that E92K affects a specific subset of acidic patch-binding proteins (Extended Data Fig. 2).

Notably, SIRT6, a deacetylase, was highly enriched in the wild-type sample, whereas the transcriptional activators, BRD2/3/4, were all enriched by E92K. Taken together, this suggests that the mutation acts to block histone lysine deacetylase activity, resulting in increased local acetylation and binding of associated reader proteins. To support this idea, we transiently expressed both wild-type and H2A E92K histones in HEK 293T cells and isolated intact mononucleosomes by anti-FLAG immunoprecipitation (Fig. 3c). We found global lysine acetylation was increased twofold in the mutant nucleosomes above wild type, with a particular increase observed on histone H4. This effect is striking given that we are probably only enriching one copy of the mutant histone per nucleosome because of presumed stochastic incorporation (Extended Data Fig. 3)^{36,37}.

Following this, we questioned whether this local increase in acetylation would lead to a global effect by weakening DNA–nucleosome interactions, leading to a more accessible chromatin environment and consequently increasing the concentration of accessible open reading frames (ORFs). To probe this, we performed ATAC-seq analysis³⁸ on HEK 293T cell lines stably expressing either wild-type H2A or the E92K mutant (Extended Data Fig. 4). Consistent with our idea, we found 5,699 ORFs which showed a significant (FDR ≤ 0.05) change in concentration across four replicates. Of these, 90% indicate regions of higher accessibility in E92K in comparison to the wild-type H2A (Fig. 3d,e and Extended Data Fig. 5), consistent with our proposed model.

We also noted that installation of E92K had a negative effect on nucleosomal DNMT3A binding (Fig. 3a). Recent structural and biochemical work has demonstrated that DNMT3 binds to the acidic patch through two arginine residues (R740 and R743 in DNMT3B)³⁹. Charge reversal mutants (for example, R740E) of these residues were shown

to diminish nucleosomal binding and de novo methylation. Our data indicate that E92K may disrupt binding in the same manner. To verify this, we performed a mononucleosome FLAG-IP from HEK 293T cells stably expressing H2A or H2A E92K and analysed the precipitated DNA for MeC (Fig. 3f). Consistent with our proposal, the data show an approximately 5% decrease in local DNA methylation in the E92K samples, supporting a model in which DNMT3 binding is impaired by E92K, leading to fewer de novo methylation events.

We were able to validate loss of function binding interactions with SIRT6, DNMT3A, INCENP (part of the CEN complex⁴⁰) and the chromatin remodeller SMARCA4 (refs. 8,41) (BRG1) using the recombinant mononucleosome assay developed by McGinty³⁵. Here, biotinylated mononucleosomes were immobilized on streptavidin beads before incubation with HEK 293T nuclear lysate. The eluent was subsequently blotted against hits from our photo-proximity labelling experiment to assess the effect of the E92K mutation on binding. In all cases, this assay supported the data presented by our μ Map experiment (Fig. 3g), with comparable enrichment values between western blot and proteomics datasets, further demonstrating that our method can accurately capture interacting proteins in an unbiased manner. Interestingly, performing the same comparative proteomics experiment with H2A/H2A(E92K)-APEX2 constructs did not reveal any differences in the interactome of mutant and wild-type samples when applying the same fold change and significance cut-offs used previously (Extended Data Figs. 6 and 10), presumably because of the increased labelling radius of the peroxidase-based platform (Extended Data Fig. 6).

Together, these data demonstrate that the resolution provided by our proximity-labelling method can be used to uncover molecular level details for gain-of-function or loss-of-function interactions in the nucleus in a single experiment.

We posited that our method could be used to determine the roles of small-molecule ligands in the chromatin micro-environment (Fig. 4a). Epigenetic drug discovery has become a critical focus for therapeutic intervention, encompassing dozens of targets across a range of therapeutic areas³. We began by examining the effects that the bromodomain inhibitor JQ-1 has on chromatin (Fig. 4b). JQ-1 is known to target the BET family of bromodomain containing readers (BRD2/3/4), with analogues progressing through the clinic^{42,43}. We theorized that μ Map would be sensitive enough to measure the effects that BRD inhibition would have on the chromosomal micro-environment. To probe this, we compared the interactomes of Ir-conjugated H2A in the presence or absence of 1 and 5 μ M JQ-1 (Fig. 4b and Extended Data Figs. 4, 7 and 10; see Supplementary Information for full data table). BRD2/3/4 were all enriched in the untreated sample ($\log_2FC > 0.5$, FDR < 0.05), consistent with blocking bromodomain–nucleosome interactions. The known JQ-1 off-target SOAT1 (ref. 44) was also enriched in the untreated sample. RNA-seq analysis of the ligand-treated cells showed that the identified interactors are not enriched on the basis of transcriptional changes associated with drug treatment (Extended Data Fig. 8).

Performing the same experiment using existing methods (APEX2, as above) showed enrichment of BRD2 and no enrichment of BRD3/BRD4 (Extended Data Fig. 7).

We then performed a similar experiment with the DOT1L methyltransferase inhibitor, pinometostat, to assess both the selectivity of this ligand and the effect that depletion of H3K79 methylation has on the chromatin micro-environment^{45,46}. DOT1L was enriched ($\log_2FC > 0.5$, FDR < 0.05) in the untreated sample, as were several proteins related to transcriptional activation, including BRD2/3/4 and POLR2E (Fig. 4c,d and Extended Data Fig. 7; see Supplementary Information for full data table). This observation is consistent with previous reports demonstrating that H3K79 methylation leads to recruitment of the acetyltransferase P300, subsequent BRD recruitment and transcriptional activation⁴⁶. It was gratifying to see that in a single experiment we can extract both target-ID data for a small-molecule ligand along with downstream transcriptional effects.

Finally, we applied our method to RNA polymerase II (POL II), which is responsible for transcribing protein-encoding genes in a highly regulated process involving the sequential association of multiple protein complexes^{47–49}. Release of promoter-proximal paused POL II is primarily achieved through phosphorylation of the disordered C-terminal domain (CTD) of the RPB1 subunit, comprised of a repeating unit of Y-S-P-T-S-P-S, by cyclin dependent kinases (CDKs). Inhibition of CDKs has therefore become an attractive therapeutic strategy to stall POL II and downregulate transcription and therefore cancer proliferation. The small-molecule ligand AT7519, a pan-CDK inhibitor, has been developed to probe this strategy in the context of multiple myeloma and is now in clinical trials⁵⁰. We questioned if we could determine how this ligand affects the POL II interactome and whether our method could unveil at what stage in its transcriptional cycle POL II is arrested by AT7519 treatment.

To assess this, we expressed RPB1-Cfa^N in HEK 293T cells, in which the intein is fused to the C terminus of the CTD (Extended Data Fig. 9). The μ Map workflow was then performed in the presence and absence of AT7519 (Fig. 4e). Comparing our treated and untreated datasets revealed CDK11, 9 and 1 to be enriched ($\log_2FC > 0.5$, FDR < 0.05) in the untreated sample, consistent with wide-ranging CDK inhibition by AT7519 (Fig. 4d; see Supplementary Information for full data table)⁵⁰. Mediator complex subunits in addition to several transcription factors were enriched in the treated sample, suggesting that CDK inhibition halts the progression of POL II at the pre-initiation complex, before CTD phosphorylation and association of the NELF and DSIF complexes⁵¹.

Conclusion

In summary, we have developed a photocatalytic proximity-labelling technology that can be deployed across the nuclear proteome. The short-range diazirine activation mechanism allows the collection of precise interactomics data that are sensitive to single amino acid mutations and can be used to detect changes caused by external stimuli such as ligand incubation. We believe this method will be broadly applicable across nuclear biology for the study of disease-associated mutations. Also, this method is an effective tool for ligand target ID in chromatin, identifying on- and off-target proteins and revealing how treatment with these molecules affects local chromatin interactomes.

Online content

Any methods, additional references, Nature Portfolio reporting summaries, source data, extended data, supplementary information, acknowledgements, peer review information; details of author contributions and competing interests; and statements of data and code availability are available at <https://doi.org/10.1038/s41586-023-05914-y>.

1. Scott, D. E., Bayly, A. R., Abell, C. & Skidmore, J. Small molecules, big targets: drug discovery faces the protein–protein interaction challenge. *Nat. Rev. Drug Discov.* **15**, 533–550 (2016).
2. Veltman, J. A. & Brunner, H. G. De novo mutations in human genetic disease. *Nat. Rev. Genet.* **13**, 565–575 (2012).
3. Campbell, R. M. & Tummino, P. J. Cancer epigenetics drug discovery and development: the challenge of hitting the mark. *J. Clin. Invest.* **124**, 64–69 (2014).
4. Geri, J. B. et al. Microenvironment mapping via Dexter energy transfer on immune cells. *Science* **367**, 1091–1097 (2020).
5. Ruffner, H., Bauer, A. & Bouwmeester, T. Human protein–protein interaction networks and the value for drug discovery. *Drug Discov. Today* **12**, 709–716 (2007).
6. Kouzarides, T. Chromatin modifications and their function. *Cell* **128**, 693–705 (2007).
7. Ganesan, A., Arimondo, P. B., Rots, M. G., Jeronimo, C. & Berdasco, M. The timeline of epigenetic drug discovery: from reality to dreams. *Clin. Epigenet.* **11**, 174 (2019).
8. Schick, S. et al. Systematic characterization of BAF mutations provides insights into intracompartmental synthetic lethality in human cancers. *Nat. Genet.* **51**, 1399–1410 (2019).
9. Cheng, F. et al. Comprehensive characterization of protein–protein interactions perturbed by disease mutations. *Nat. Genet.* **53**, 342–353 (2021).
10. Cheng, Y. et al. Targeting epigenetic regulators for cancer therapy: mechanisms and advances in clinical trials. *Signal Transduct. Target. Ther.* **4**, 62 (2019).
11. Weinberg, D. N., Allis, C. D. & Lu, C. Oncogenic mechanisms of histone H3 mutations. *Cold Spring Harb. Perspect. Med.* **7**, a026443 (2017).

12. Bagert, J. D. et al. Oncohistone mutations enhance chromatin remodeling and alter cell fates. *Nat. Chem. Biol.* **17**, 403–411 (2021).
13. Nacev, B. A. et al. The expanding landscape of ‘oncohistone’ mutations in human cancers. *Nature* **567**, 473–478 (2019).
14. Müller, M. M. & Muir, T. W. Histones: at the crossroads of peptide and protein chemistry. *Chem. Rev.* **115**, 2296–2349 (2015).
15. Vermeulen, M. & Déjardin, J. Locus-specific chromatin isolation. *Nat. Rev. Mol. Cell Biol.* **21**, 249–250 (2020).
16. Van Mierlo, G. & Vermeulen, M. Chromatin proteomics to study epigenetics—challenges and opportunities. *Mol. Cell. Proteomics* **20**, 100056 (2021).
17. Ciferri, C. et al. Molecular architecture of human polycomb repressive complex 2. *eLife* **1**, e00005 (2012).
18. Ruthenburg, A. J. et al. Recognition of a mononucleosomal histone modification pattern by BPTF via multivalent interactions. *Cell* **145**, 692–706 (2011).
19. Zhao, S., Yue, Y., Li, Y. & Li, H. Identification and characterization of ‘readers’ for novel histone modifications. *Curr. Opin. Chem. Biol.* **51**, 57–65 (2019).
20. Burton, A. J. et al. In situ chromatin interactomics using a chemical bait and trap approach. *Nat. Chem.* **12**, 520–527 (2020).
21. Kleiner, R. E., Hang, L. E., Molloy, K. R., Chait, B. T. & Kapoor, T. M. A chemical proteomics approach to reveal direct protein–protein interactions in living cells. *Cell Chem. Biol.* **25**, 110–120 (2018).
22. Seath, C. P., Trowbridge, A. D., Muir, T. W. & MacMillan, D. W. C. Reactive intermediates for interactome mapping. *Chem. Soc. Rev.* **50**, 2911–2926 (2021).
23. Villaseñor, R. et al. ChromID identifies the protein interactome at chromatin marks. *Nat. Biotechnol.* **38**, 728–736 (2020).
24. Ummethum, H. & Hamperl, S. Proximity labeling techniques to study chromatin. *Front. Genet.* **11**, 450 (2020).
25. Baldi, S., Korber, P. & Becker, P. B. Beads on a string—nucleosome array arrangements and folding of the chromatin fiber. *Nat. Struct. Mol. Biol.* **27**, 109–118 (2020).
26. Stevens, A. J. et al. A promiscuous split intein with expanded protein engineering applications. *Proc. Natl Acad. Sci. USA* **114**, 8538–8543 (2017).
27. Stevens, A. J. et al. Design of a split intein with exceptional protein splicing activity. *J. Am. Chem. Soc.* **138**, 2162–2165 (2016).
28. Scott, W. A. & Campos, E. I. Interactions with histone H3 & tools to study them. *Front. Cell Dev. Biol.* **8**, 701 (2020).
29. Pan, D. et al. Mechanism of centromere recruitment of the CENP-A chaperone HJURP and its implications for centromere licensing. *Nat. Commun.* **10**, 4046 (2019).
30. Chen, C. C. et al. Establishment of centromeric chromatin by the CENP-A assembly factor CAL1 requires FACT-mediated transcription. *Dev. Cell* **34**, 73–84 (2015).
31. Bennett, R. L. et al. A mutation in histone H2B represents a new class of oncogenic driver. *Cancer Discov.* **9**, 1438–1451 (2019).
32. McGinty, R. K. & Tan, S. Nucleosome structure and function. *Chem. Rev.* **115**, 2255–2273 (2015).
33. McBride, M. J. et al. The nucleosome acidic patch and H2A ubiquitination underlie mSWI/SNF recruitment in synovial sarcoma. *Nat. Struct. Mol. Biol.* **27**, 836–845 (2020).
34. Dao, H. T., Dul, B. E., Dann, G. P., Liszczak, G. P. & Muir, T. W. A basic motif anchoring ISWI to nucleosome acidic patch regulates nucleosome spacing. *Nat. Chem. Biol.* **16**, 134–142 (2020).
35. Skrajna, A. et al. Comprehensive nucleosome interactome screen establishes fundamental principles of nucleosome binding. *Nucleic Acids Res.* **48**, 9415–9432 (2020).
36. Anink-Groenen, L. C. M., Maarleveld, T. R., Verschure, P. J. & Bruggeman, F. J. Mechanistic stochastic model of histone modification pattern formation. *Epigenetics Chromatin* **7**, 30 (2014).
37. Tachiwana, H. et al. Chromatin structure-dependent histone incorporation revealed by a genome-wide deposition assay. *eLife* **10**, e66290 (2021).
38. Grandi, F. C., Modi, H., Kampman, L. & Corces, M. R. Chromatin accessibility profiling by ATAC-seq. *Nat. Protoc.* **17**, 1518–1552 (2022).
39. Xu, T. et al. Structure of nucleosome-bound DNA methyltransferases DNMT3A and DNMT3B. *Nature* **586**, 151–155 (2020).
40. Bolton, M. A. et al. Aurora B kinase exists in a complex with survivin and INCENP and its kinase activity is stimulated by survivin binding and phosphorylation. *Mol. Biol. Cell* **13**, 3064–3077 (2002).
41. Hodges, C., Kirkland, J. G. & Crabtree, G. R. The many roles of BAF (mSWI/SNF) and PBAF complexes in cancer. *Cold Spring Harb. Perspect. Med.* **6**, a026930 (2016).
42. Filippakopoulos, P. et al. Selective inhibition of BET bromodomains. *Nature* **468**, 1067–1073 (2010).
43. Shi, J. & Vakoc, C. R. The mechanisms behind the therapeutic activity of BET bromodomain inhibition. *Mol. Cell* **54**, 728–736 (2014).
44. Savitski, M. M. et al. Multiplexed proteome dynamics profiling reveals mechanisms controlling protein homeostasis. *Cell* **173**, 260–274 (2018).
45. Stein, E. M. et al. The DOT1L inhibitor pinometostat reduces H3K79 methylation and has modest clinical activity in adult acute leukemia. *Blood* **131**, 2662–2669 (2018).
46. Gilan, O. et al. Functional interdependence of BRD4 and DOT1L in MLL leukemia. *Nat. Struct. Mol. Biol.* **23**, 673–681 (2016).
47. Osman, S. & Cramer, P. Structural biology of RNA polymerase II transcription: 20 years on. *Annu. Rev. Cell Dev. Biol.* **36**, 1–34 (2020).
48. Cramer, P. Organization and regulation of gene transcription. *Nature* **573**, 45–54 (2019).
49. Young, R. A. RNA polymerase II. *Annu. Rev. Biochem.* **60**, 689–715 (1991).
50. Santo, L. et al. AT7519, a novel small molecule multi-cyclin-dependent kinase inhibitor, induces apoptosis in multiple myeloma via GSK-3B activation and RNA polymerase II inhibition. *Oncogene* **29**, 2325–2336 (2010).
51. Harlen, K. M. & Churchman, L. S. The code and beyond: transcription regulation by the RNA polymerase II carboxy-terminal domain. *Nat. Rev. Mol. Cell Biol.* **18**, 263–273 (2017).

Publisher's note Springer Nature remains neutral with regard to jurisdictional claims in published maps and institutional affiliations.

Springer Nature or its licensor (e.g. a society or other partner) holds exclusive rights to this article under a publishing agreement with the author(s) or other rightsholder(s); author self-archiving of the accepted manuscript version of this article is solely governed by the terms of such publishing agreement and applicable law.

© The Author(s), under exclusive licence to Springer Nature Limited 2023

Methods

Solid-phase peptide synthesis

Boc-N^α-Cfa^C-CFGSGK(alloc)-G-NH₂ was synthesized on a 0.1 mmol scale by standard Fmoc solid-phase peptide synthesis using DIC-Oxyma activation on a CEM Liberty Blue microwave-assisted peptide synthesizer on ChemMatrix Rink amide resin. Each residue was double coupled during the synthesis. Fmoc deprotection was performed at room temperature by the addition of 20% piperidine in dimethylformamide (DMF) with 0.1 M hydroxybenzotriazole. Alloc deprotection was performed by the addition of 0.1 equivalent (equiv.) Pd(PPh₃)₄ and 2.5 equiv. *N,N'*-dimethylbarbituric acid in dichloromethane (DCM) with nitrogen agitation. Treatment was performed twice at room temperature for 30 min. The resin was sequentially washed with 3× DCM, 3× DCM:DMF (1:1 v/v), 3× DMF and 1× 5% w/v sodium diethyldithiocarbamate in DMF.

The resin was then split into 0.02 mmol aliquots and treated as follows. Cfa^C-biotin: biotin (5 equiv.) was coupled to the deprotected lysine side chain with PyAOP (4.95 equiv.) and *N,N*-diisopropylethylamine (DIEA) (10 equiv.) activation in NMP for 4 h with nitrogen agitation. The resin was washed with 3× NMP, 3× DMF and 3× DCM. Side-chain deprotection and cleavage from the resin was affected by addition of a 92.5:2.5:2.5:2.5 v/v/v solution of TFA:TIPS:EDT:H₂O for 130 min at room temperature. The cleavage solution was reduced to less than 5 ml volume under a positive pressure of N₂ and the crude peptide was precipitated using cold diethyl ether. The crude peptide was isolated by refrigerated centrifugation, resuspended in 50/50 v/v H₂O:MeCN with 0.1% TFA and lyophilized to yield a white solid. Cfa^C-Ir: the iridium photocatalyst⁵² was conjugated to the deprotected lysine side chain by treatment with NHS-Ir (1.2 equiv.) and DIEA (2 equiv.) in DMF for 2 h with nitrogen agitation in the absence of light. The resin was washed with 3× DMF and 3× DCM. Side-chain deprotection and cleavage from the resin was affected by addition of a 95:2.5:2.5 v/v/v solution of TFA:TIPS:H₂O for 130 min at room temperature in the absence of light. The cleavage solution was reduced to less than 5 ml volume under a positive pressure of N₂ and the crude peptide was precipitated using cold diethyl ether. The crude peptide was isolated by refrigerated centrifugation, resuspended in 50/50 v/v H₂O:MeCN with 0.1% TFA and lyophilized to yield a pale yellow solid.

Crude lyophilized peptides were purified by preparative scale reversed-phase high-performance liquid chromatography and characterized by mass spectrometry.

Cell culture

HEK 293T cells were cultured as a monolayer in DMEM (Thermo Fisher), supplemented with 10% v/v FBS (Thermo Fisher), 100 U ml⁻¹ of penicillin (Thermo Fisher) and 100 μg ml⁻¹ of streptomycin (Thermo Fisher). Cells were maintained in an incubator at 37 °C with 5% CO₂.

Each 10 cm plate of HEK 293T cells at 70% confluency was transfected with a plasmid encoding POI-HA-Cfa^N-FLAG (5 μg per plate) with lipofectamine 2000 (12 μl per plate) following the manufacturer's instructions. After 6 h, the medium was aspirated and replaced with fresh medium. Transfection was performed for 24 or 48 h in an incubator at 37 °C with 5% CO₂.

Protein *trans*-splicing for TMT-10-plex experiments

A total of 3 × 10⁷ HEK 293T cells transfected with POI-HA-Cfa^N-FLAG were lysed by hypotonic lysis in 3 ml of RSB buffer (10 mM Tris buffer, 15 mM NaCl, 1.5 mM MgCl₂, Roche cOmplete EDTA-free protease inhibitors, pH 7.6) for 10 min on ice. The crude nuclei were isolated by centrifugation at 400g for 5 min at 4 °C. The nuclei were resuspended in 3 ml of RSB buffer and homogenized with ten strokes of a loose pestle Dounce homogenizer and pelleted at 400g for 5 min at 4 °C. The nuclei were resuspended in cross-linking buffer (20 mM HEPES, 1.5 mM MgCl₂, 150 mM KCl, Roche cOmplete EDTA-free protease inhibitors, pH 7.6)

and centrifuged at 400g for 5 min at 4 °C. Finally, the nuclei were resuspended in 300 μl of cross-linking buffer per 1 × 10⁷ cells. To the isolated nuclei was added Cfa^C-Ir in cross-linking buffer (0.5 μM final concentration). The nuclei were incubated at 37 °C for 1 h.

The nuclei were isolated by centrifugation at 400g for 5 min at 4 °C and washed twice with cross-linking buffer (500 μl) to remove excess peptide. The pellets were then resuspended in 3 ml of cross-linking buffer containing diazirine–biotin conjugate (200 μM) and irradiated with blue light for between 45 and 90 s in the Penn PhD Photoreactor M2 at 100% light intensity at 4 °C. The nuclei were re-isolated by centrifugation at 400g for 5 min at 4 °C and washed once with cross-linking buffer to remove excess biotin–diazirine. The washed pellets were then resuspended in 2 ml of LB3 buffer (10 mM Tris, 100 mM NaCl, 1 mM EDTA, 0.5 mM EGTA, 0.1% sodium deoxycholate, 0.5% sodium lauroyl sarcosinate, pH 7.5) and sonicated using a Branson probe tip sonicator (12 cycles at 25% amplitude, 15 s on 15 s off on ice).

The lysed nuclei were then clarified through centrifugation at 15,000g for 20 min at 4 °C and the protein concentration of the supernatant was determined by BCA assay. Protein concentration was normalized across all experimental replicates and diluted to 1 mg ml⁻¹ with binding buffer (25 mM Tris, 150 mM NaCl, 0.25% v/v NP-40, pH 7.5). Then 1 ml of each sample was incubated with 125 μl of prewashed magnetic Sepharose streptavidin beads (<https://www.cytivalifesciences.com>, no. 28985738) for 2 h at room temperature with end-over-end rotation. The beads were subsequently washed twice with 1% w/v SDS in PBS, twice with 1 M NaCl in PBS and 10% ethyl alcohol in PBS ×3.

Experiments with ligand treatment

Following transfection, plated cells expressing POI-HA-Cfa^N-FLAG were treated with the small-molecule ligand for the specified amount of time (Supplementary Table 2). Following this, cells were scraped and pelleted as described previously. All buffers used in cell processing before irradiation (RSB, cross-linking) contained the ligand. Following irradiation, samples were treated as normal.

For proteomic analysis

Following streptavidin enrichment, the beads were resuspended in PBS (300 μl) and transferred to a new 1.5 ml LoBind tube. The supernatant was removed and the beads were washed with 3× PBS (0.5 ml) and 3× ammonium bicarbonate (100 mM).

The beads were resuspended in 500 μl of 3 M urea in PBS and 25 μl of 200 mM dithiothreitol in 25 mM NH₄HCO₃ was added. The beads were incubated at 55 °C for 30 min. Subsequently, 30 μl of 500 mM iodoacetamide in 25 mM NH₄HCO₃ was added and incubated for 30 min at room temperature in the dark. The supernatant was removed and the beads washed with 3× 0.5 ml of DPBS and 6× 0.5 ml of triethyl ammonium bicarbonate (TEAB, 50 mM). The beads were resuspended in 0.5 ml of TEAB (50 mM) and transferred to a new protein LoBind tube. The beads were resuspended in 40 μl of TEAB (50 mM), 1.2 μl of trypsin (1 mg ml⁻¹ in 50 mM acetic acid) was added and the beads incubated overnight with end-over-end rotation at 37 °C. After 16 h, a further 0.8 μl of trypsin was added and the beads were incubated for an extra 1 h at 37 °C. Meanwhile, TMT-10-plex label reagents (0.8 mg) (Thermo) were equilibrated to room temperature and diluted with 40 μl of anhydrous acetonitrile (Optima grade; 5 min with vortexing) and centrifuged. A total of 40 μl of each TMT reagent was added to the appropriate sample. The reaction was incubated for 2 h at room temperature. The samples were quenched with 8 μl of 5% hydroxylamine and incubated for 15 min. The samples were pooled in a new Protein LoBind tube and acidified with TFA (16 μl, Optima).

Mass spectra were obtained using an Orbitrap Fusion Lumos mass spectrometer at Princeton Proteomics Facility and analysed using MaxQuant⁵³. TMT-labelled peptides were dried down in a SpeedVac, redissolved in 300 μl of 0.1% TFA in water and fractionated into eight fractions using the Pierce High pH Reversed-Phase Peptide

Fractionation Kit (no. 84868). Resulting MS/MS/MS data were searched in Maxquant against the Uniprot human protein database containing common contaminants. The proteinGroups.txt file was subsequently imported into Perseus (<https://maxquant.net/perseus/>)⁵⁴. The data were then filtered on the basis of the following criteria, 'only identified by site', 'reverse' and 'potential contaminant'. The resulting data were log₂-transformed and median normalization was performed. FDR-corrected *P* values were determined by a two-sample *t*-test following the Benjamini–Hochberg procedure. The data were visualized by plotting as a volcano plot.

Procedure for mononucleosome IP

Two 10 cm plates of HEK 293T cells transfected with H2A-E92K-HA-Cfa^N-FLAG (approximately 30 million cells) and two 10 cm plates of HEK 293T cells transfected with H2A-HA-Cfa^N-FLAG (approximately 30 million cells) were lysed in 1 ml of hypotonic lysis buffer (10 mM Tris, 15 mM NaCl, 1.5 mM MgCl₂, Roche cOmplete EDTA-free protease inhibitors, 1 mM dithiothreitol, 5 mM sodium butyrate, pH 7.6) for 10 min on ice and the nuclei were pelleted at 400g for 5 min at 4 °C. The nuclei were then resuspended in RSB + 1 mM dithiothreitol + 0.2% v/v Triton X-100 + 5 mM Na butyrate (500 µl per condition) and incubated on ice for 5 min. Nuclei were then pelleted at 400g for 5 min at 4 °C. The nuclei were washed once more with RSB + 1 mM dithiothreitol + 5 mM Na butyrate and centrifuged at 600g for 5 min at 4 °C.

The nuclei were then resuspended in 500 µl of MNase digestion buffer (10 mM Tris, 60 mM KCl, 15 mM NaCl, 2 mM CaCl₂, pH 7.5) and were incubated at 37 °C for 10 min. MNase (5 µl, NEB) was then added to each condition for 10 min at 37 °C (digestion time varies by enzyme batch and must be determined for each experiment. A total of 2 µl of the digest was removed every 2 min and quenched by addition of 20 mM EGTA. These aliquots were run on a 1.2% agarose gel and the digestion efficiency visualized with ethidium bromide staining). Once digestion to mononucleosomes was complete, the reaction was quenched with the addition of 20 mM EGTA on ice for 5 min. The sample was spun at 1,300g for 5 min at 4 °C and the supernatant was collected (fraction S1). A total of 500 µl of buffer TE + 5 mM Na butyrate (10 mM Tris, 1 mM EDTA, pH 8.0) was added to the pellet and the sample was rotated end-over-end at 4 °C for 30 min. The sample was spun at 13,000g for 5 min at 4 °C and the supernatant was collected (fraction S2). To 475 µl of S1 was added 475 µl of 2× buffer E (30 mM HEPES, 225 mM NaCl, 3 mM MgCl₂, 0.4% Triton X-100, 20% v/v glycerol, pH 7.5) with constant vortexing dropwise for 1 min. To 475 µl of S2 was added 237 µl of 3× buffer D (60 mM HEPES, 450 mM NaCl, 4.5 mM MgCl₂, 0.6 mM EGTA, 0.6% Triton X-100, 30% v/v glycerol, pH 7.5) with constant vortexing dropwise for 1 min. The samples were spun at 13,000g for 5 min at 4 °C. The two fractions were combined in a 5 ml LoBind Eppendorf tube and 30 µl of magnetic FLAG beads (Sigma M2 anti-FLAG magnetic beads; prewashed with 1× buffer D) were added per condition. The FLAG-IP was performed overnight with end-over-end rotation at 4 °C.

The beads were washed sequentially with 1× buffer D and 1× buffer D + 0.5% v/v Triton X-100 for 2 min each with rotation. A total of 40 µl of 1× SDS loading buffer was added and the beads were boiled for 10 min. Samples were run on a 15% Tris gel for western blotting with appropriate antibodies.

Procedure for assaying local DNA methylation

Mononucleosome isolation was performed as above from HEK 293T cells stably expressing H2A-HA-Cfa^N-FLAG or H2A-E92K-HA-Cfa^N-FLAG. Following this, mononucleosomes were enriched using 30 µl of magnetic FLAG beads (Sigma M2 anti-FLAG magnetic beads; prewashed with 1× buffer D) per condition. The FLAG-IP was performed overnight with end-over-end rotation at 4 °C.

The beads were washed sequentially with 1× buffer D and 1× buffer D + 0.5% v/v Triton X-100 for 2 min each with rotation. The beads were then washed twice with TE and resuspended in 200 µl of elution buffer

(50 mM Tris-Cl (pH 8.0), 10 mM EDTA, 1% SDS) supplanted with 1 µl of proteinase K (20 µg µl⁻¹). The samples were rotated at 55 °C for 2 h. Following this, the samples were centrifuged at 10×1,000g for 1 min before being pelleted on a magnetic rack. The supernatants were transferred to clean LoBind tubes. The beads were then resuspended in 100 µl of elution buffer supplanted with 1 µl of proteinase K (20 µg µl⁻¹) and rotated at 55 °C for a further 2 h. Again, the samples were centrifuged at 10,000g for 1 min before being pelleted on a magnetic rack and the supernatants transferred to clean LoBind tubes. The supernatants were combined (in each replicate) and the eluted DNA was purified using a Monarch PCR & DNA Cleanup Kit according to the manufacturer's instructions.

The eluted DNA was then digested using the Nucleoside Digestion Mix (NEB: M0649S) following the manufacturer's instructions. Digested nucleotide mixtures were then analysed by MS and the ratio of dC to methylated dC was calculated and normalized to global methylation levels. Briefly, LC–QQQ–MS quantitation of digested deoxynucleosides was performed following literature precedent⁵⁵ using a dynamic multiple reaction monitoring method on an Agilent 1260 LC Infinity II system coupled to an Agilent 6470 triple quadrupole mass spectrometer in positive ion mode. An InfinityLab Poroshell 120 SB C18 Column (Agilent, 683775-906(T), 2.7 µm particle size, 2.1 × 150 mm²) was used for all analyses with a gradient composed of 0.1% formic acid in water (A) and acetonitrile (B) at 0.4 ml min⁻¹ flow rate. The following mass spectrometer operating parameters were used: gas temperature 325 °C, gas flow rate 12 l min⁻¹, nebulizer pressure 20 p.s.i., capillary voltage 2,500 V and fragmentor voltage 70 V; collision energy was set to 14 for dC and 7 for m5dC. The MS1 (parent ion) to MS2 (deglycosylated base ion) transition for dC was set to *m/z* 228.1→112 and *m/z* 242.1→126 for m5dC. Commercially available deoxyribonucleosides were used to generate standard curves and the concentration of m5dC was normalized to dC concentration. Data quantification was performed with Agilent MassHunter Workstation Data Acquisition v.10.0.6.

Subcellular fractionation

One 10 cm plate of HEK 293T cells was transfected with the denoted plasmids and these were collected as previously described. Cells were lysed in hypotonic lysis buffer (10 mM Tris, 15 mM NaCl, 1.5 mM MgCl₂, PI, pH 7.6) on ice for 10 min, followed by centrifugation at 400g for 5 min at 4 °C. The supernatant was removed (cytosolic fraction) and the pellet was resuspended in hypotonic lysis buffer + 1% v/v Triton X-100. Nuclei were lysed with ten strokes of a tight pastel homogenizer followed by centrifugation at 10,000g for 10 min at 4 °C. The supernatant was removed (nucleoplasmic fraction) and RIPA buffer was added to the pellet. The sample was sheared by probe sonication (2 × 10 s total, 25% amplitude, 1 s on, 1 s off) to yield the chromatin fraction. SDS loading buffer was added and the samples were analysed by western blotting using the indicated antibodies.

Recombinant nucleosome immunoprecipitation

Nuclear lysate was prepared as before. Following this, biotinylated nucleosomes (<https://www.epicypher.com/products/nucleosomes/mutant-nucleosomes/>) were immobilized on streptavidin T1 magnetic dynabeads (MyOne, Thermo Fisher) in BB150 (20 mM HEPES pH 7.5, 150 mM NaCl, 10% glycerol, 1 mM dithiothreitol, 0.1% NP-40) by rotation for 2 h at 4 °C. A total of 60 µg of nucleosomes were incubated with 150 µl of resuspended resin in 1 ml of BB150. Streptavidin-bound nucleosomes were rinsed twice and washed for 30 min by rotating with 1 ml of BB150 at 4 °C and divided equally into three tubes. Nuclear lysate (700 µg) was mixed with 300 µl of BB150 and centrifuged at 10,000g for 10 min at 4 °C before adding to nucleosome-bound streptavidin beads.

The mixture was rotated for 2 h at 4 °C after which the beads were rinsed twice with 0.5 ml of BB150 and then rotated for 1 h at 4 °C with 0.5 ml of BB150. Washed dynabeads were moved to new tubes with about

Article

500 µl of BB150, the beads were pelleted on a magnetic rack and the buffer was aspirated, washed beads were then centrifuged at 800g for 2 min at 4 °C and aspirated again to remove residual buffer. Beads were then resuspended in 15 µl of 2× gel loading buffer (Bio-Rad) and boiled for 5 min before being pelleted on a magnetic rack. Eluted proteins were then analysed by western blotting using the indicated antibodies.

ATAC-seq analysis

ATAC-seq analysis was performed by Genewiz. Briefly, cells stably expressing H2A-HA-Cfa^N-FLAG or H2A(E92K)-HA-Cfa^N-FLAG were collected and cryopreserved before delivery to Genewiz for analysis. Both conditions were analysed over four biological replicates.

RNA-seq analysis

RNA-seq analysis was performed by Genewiz. Briefly, cells stably expressing H2A-HA-Cfa^N-FLAG were treated with either JQ-1 (1 µM for 3 h) or pinometostat (2.5 µM for 24 h) collected and cryopreserved before delivery to Genewiz for analysis. Four biological replicates were performed for each condition.

Generation of stable cell lines

Constructs were cloned into a pCDH-CMV-MCS-EF1-Puro expression vector using standard restriction cloning procedures. Lentiviral cell lines were generated using established methods.

Statistics and reproducibility

Statistical analyses were performed using Prism (GraphPad). *P* values were determined by paired *t*-tests as appropriate and as listed in the figure legends. The statistical significances of differences (**P* < 0.05, ***P* < 0.01, ****P* < 0.001, *****P* < 0.0001) are specified throughout the figures and legends. We analysed GO using Metascape⁵⁶. Heatmap was generated using Heatmapper (Heatmapper.ca)⁵⁷. Expression and splicing blots were repeated successfully three times. Proteomics experiments in Figs. 2h, 3a, 4b, 4c and 4f have been performed once.

Reporting summary

Further information on research design is available in the Nature Portfolio Reporting Summary linked to this article.

Data availability

All relevant data are included in the manuscript and Supplementary Information. Mass spectrometry data files have been uploaded to the Massive proteomics database PXD038956 (<ftp://massive.ucsd.edu/MSV000090929/>). Sequencing data are available on the GEO database (GSE221674).

52. Trowbridge, A. D. et al. Small molecule photocatalysis enables drug target identification via energy transfer. *Proc. Natl Acad. Sci. USA* **119**, e2208077119 (2022).
53. Cox, J. & Mann, M. MaxQuant enables high peptide identification rates, individualized p.p.b.-range mass accuracies and proteome-wide protein quantification. *Nat. Biotechnol.* **26**, 1367–1372 (2008).
54. Tyanova, S. et al. The Perseus computational platform for comprehensive analysis of (prote)omics data. *Nat. Methods* **13**, 731–740 (2016).
55. Traube, F. R. et al. Isotope-dilution mass spectrometry for exact quantification of noncanonical DNA nucleosides. *Nat. Protoc.* **14**, 283–312 (2019).
56. Zhou, Y. et al. Metascape provides a biologist-oriented resource for the analysis of systems-level datasets. *Nat. Commun.* **10**, 1523 (2019).
57. Babicki, S. et al. Heatmapper: web-enabled heat mapping for all. *Nucleic Acids Res.* **44**, 147–153 (2016).

Acknowledgements Research reported in this publication was supported by the NIH National Institute of General Medical Sciences (R35GM134897-01, R01-GM103558-03 and R37-GM086868) and the NIH National Cancer Institute (P01 CA196539). A.J.B. was a Damon Runyon Fellow of the Damon Runyon Cancer Research Foundation (DRG-2283-17). We thank S. Kyin and H. H. Shwe at the Princeton Proteomics Facility. The mock volcano plot in Fig. 1 was created using BioRender.

Author contributions C.P.S., A.J.B., T.W.M. and D.W.C.M. conceived the work. C.P.S., A.J.B., X.S., G.L., R.E.K., T.W.M. and D.W.C.M. designed and executed the experiments. C.P.S., A.J.B., T.W.M. and D.W.C.M. prepared this manuscript.

Competing interests A provisional US patent has been filed by D.W.C.M. and C.P.S. on the basis of photocatalysts used in this work, 62/982,366 and 63/076,658, international application no. PCT/US2021/019959. D.W.C.M. declares an ownership interest and C.P.S. declares an affiliation interest in the company Dexterity Pharma LLC, which has commercialized materials used in this work. The remaining authors declare no competing interests.

Additional information

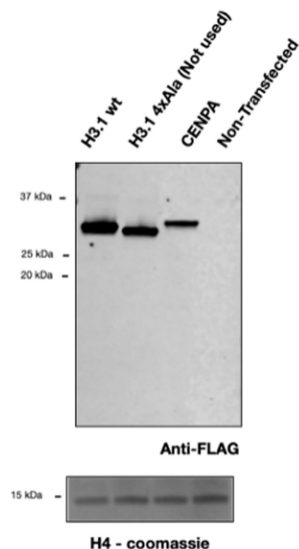
Supplementary information The online version contains supplementary material available at <https://doi.org/10.1038/s41586-023-05914-y>.

Correspondence and requests for materials should be addressed to David W. C. MacMillan or Tom W. Muir.

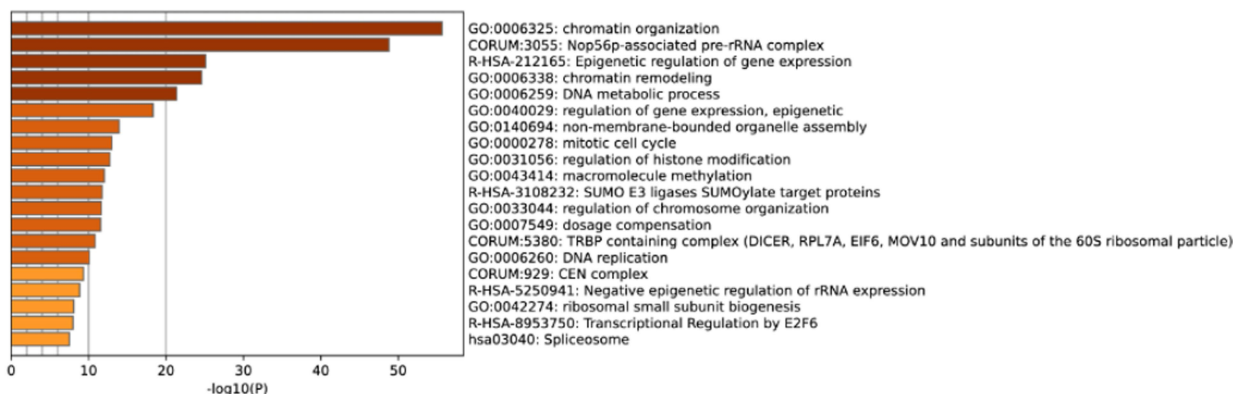
Peer review information Nature thanks Stephen Frye, Michiel Vermeulen and the other, anonymous, reviewer(s) for their contribution to the peer review of this work.

Reprints and permissions information is available at <http://www.nature.com/reprints>.

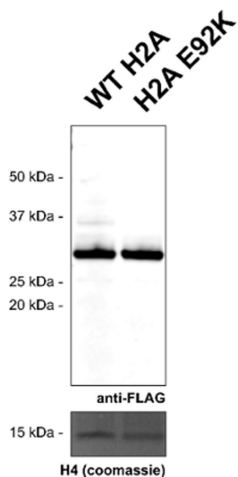
A)



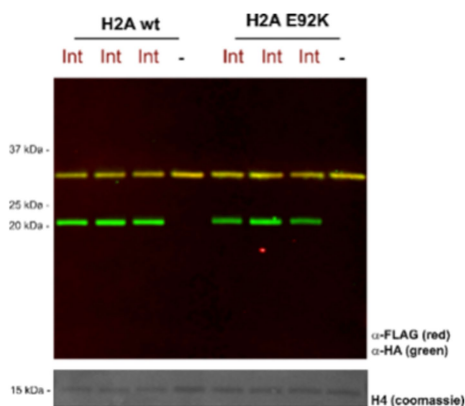
B)



C)

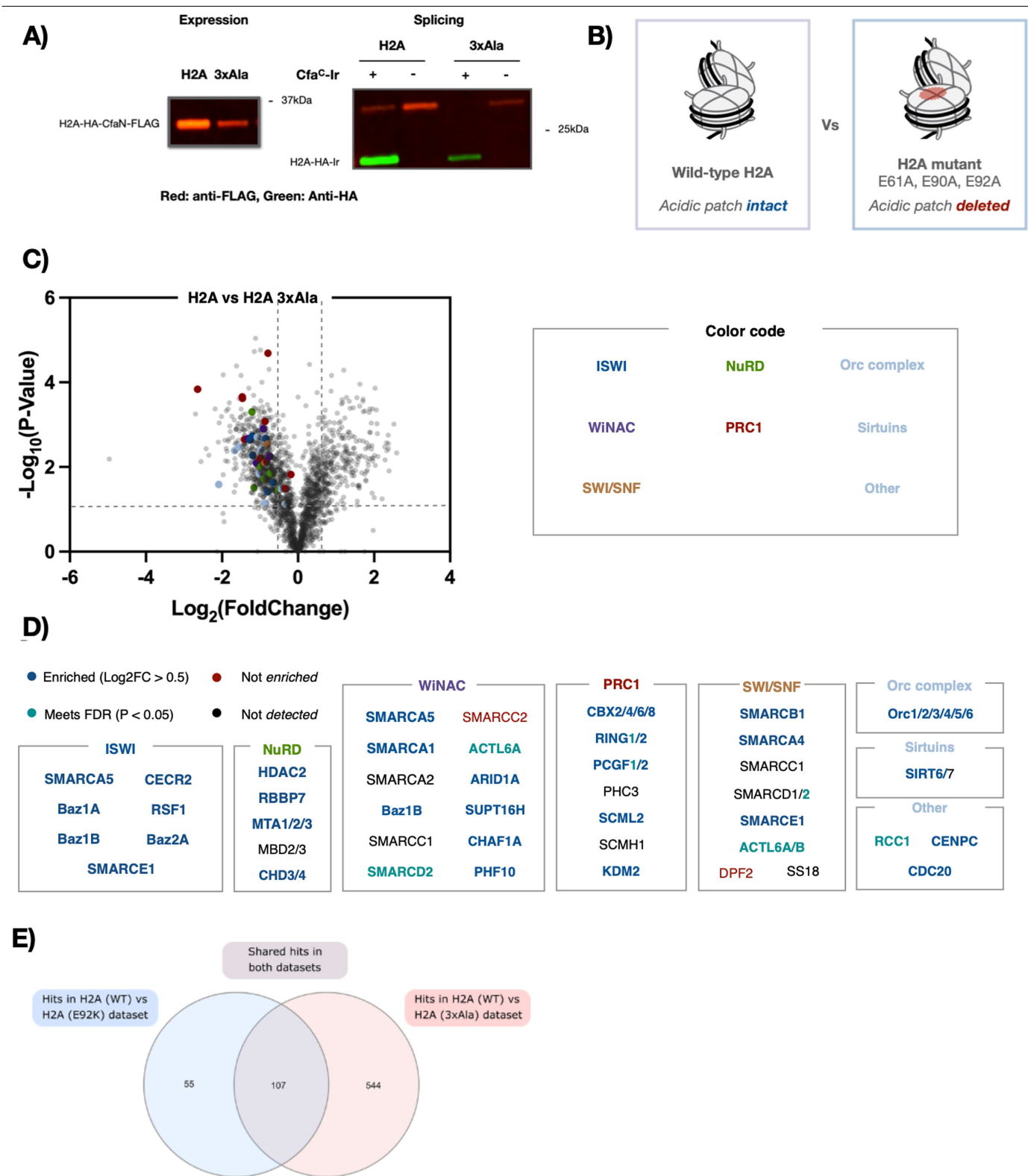


D)



Extended Data Fig. 1 | Supporting data for H3.1 vs CENP-A and H2A WT vs H2A E92K experiments. Anti-FLAG western blot for the expression of H3.1-HA-Cfa^N-FLAG, H3.1 (4xAla)-HA-Cfa^N-FLAG (not used in MS experiment) and CENP-A-HA-Cfa^N-FLAG. H4 visualized by coomassie blue stain is provided as a loading control. MW of H3.1-HA-Cfa^N-FLAG = 29,365 Da. B) GO analysis of proteins enriched in H3.1 samples. Data shows significant GO terms related to Chromatin organization, remodelling, and epigenetic control of gene expression. Analysis performed using metascap. C) Anti-FLAG western blot

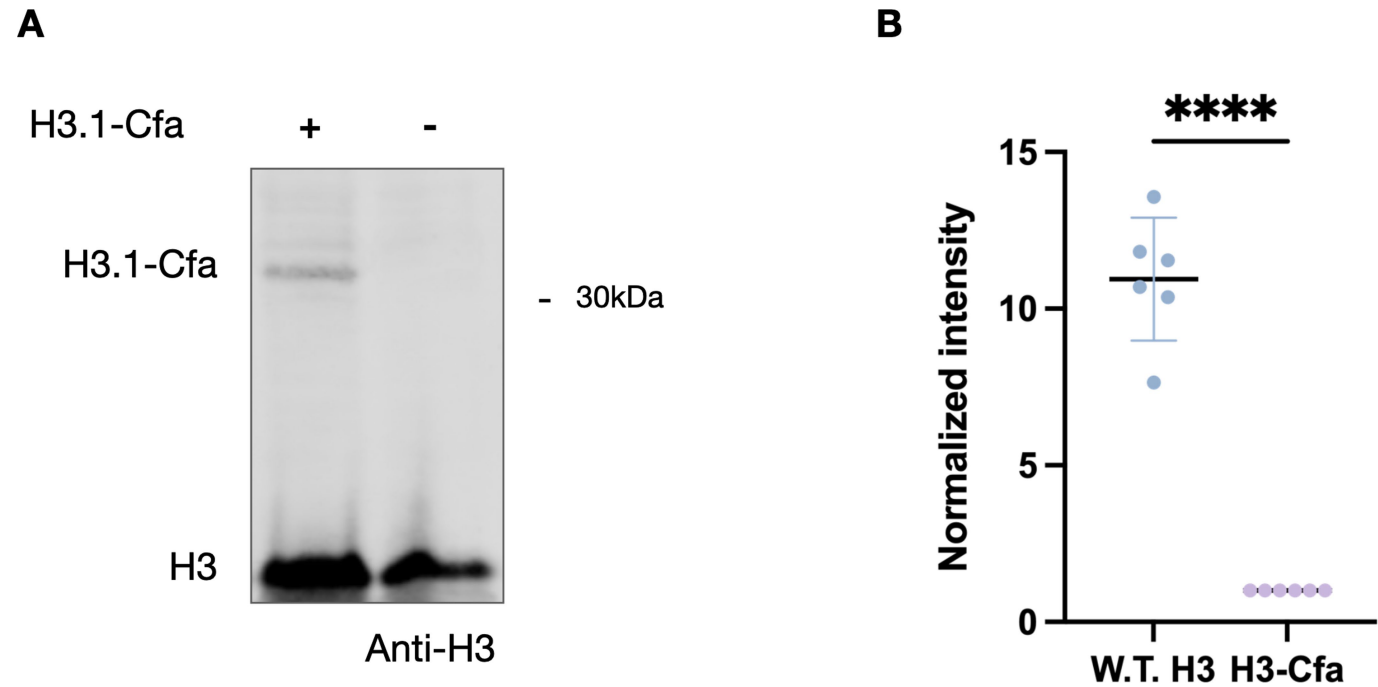
for the expression of H2A-HA-Cfa^N-FLAG and H2A-E92K-HA-Cfa^N-FLAG. H4 visualized by coomassie blue stain is provided as a loading control. D) In-nuclei splicing reactions for H2A (WT) and H2A (E92K) constructs in the presence of Cfa^C-Ir (referred to as Int) and control as visualized by anti-HA and anti-FLAG western blot. H4 visualized by coomassie blue stain is provided as a loading control. MW of H2A-HA-Cfa^N-FLAG = 28,121 Da. For blot source data, see Supplementary Fig. 1.



Extended Data Fig. 2 | See next page for caption.

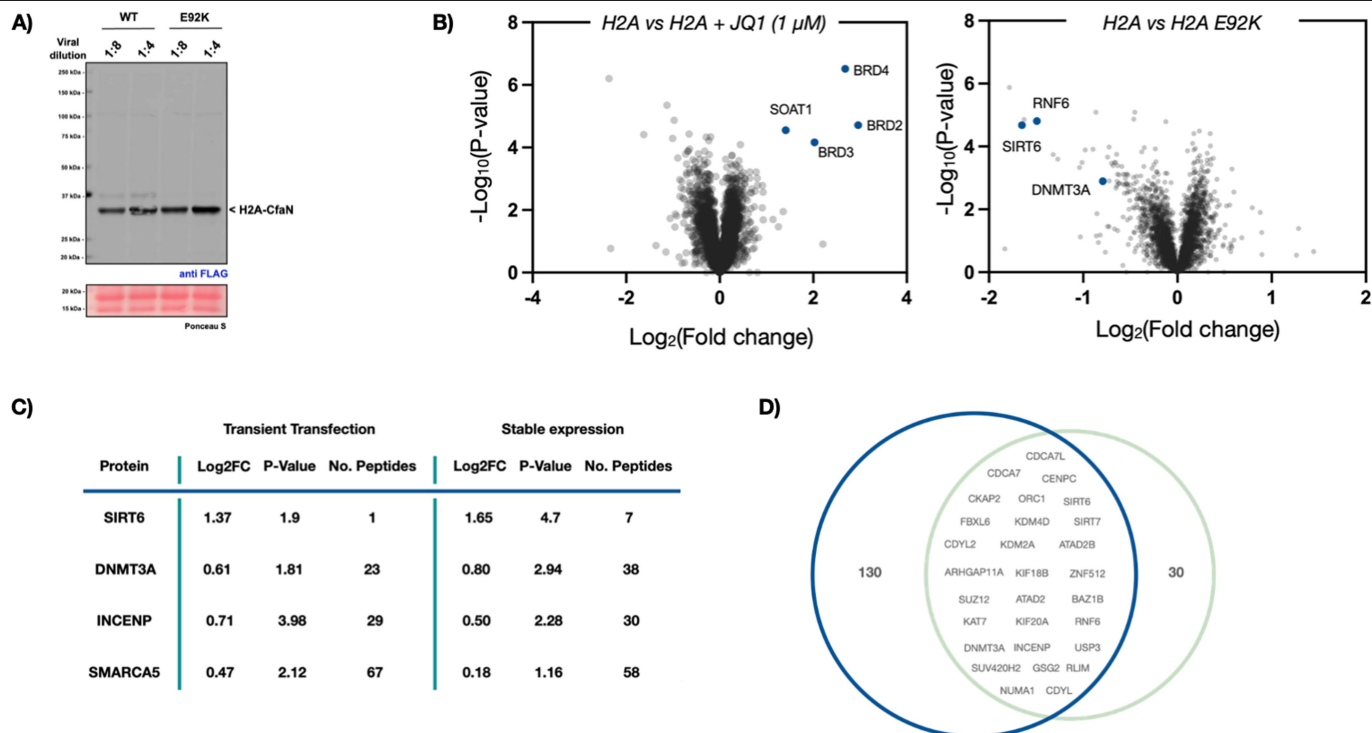
Extended Data Fig. 2 | Interactome of acidic patch triple mutant and comparison to H2A E92K. A) Left: Anti-FLAG western blot for the expression of H2A-HA-Cfa^N-FLAG and H2A-3xAla-HA-Cfa^N-FLAG. Note, 3xAla refers to the acidic patch mutations E61A, E90A and E92A in H2A. Right: In-nuclei splicing reactions for H2A (WT) and H2A (3xAla) constructs in the presence of Cfa^C-Ir as visualized by anti-HA and anti-FLAG western blot. B) Graphic representing a comparative experiment between H2A (WT) and H2A (3xAla). C) Volcano plot derived from a two-sided t-test showing proteins enriched in a comparative proteomics study between H2A (WT) and H2A (3xAla) using the μ Map workflow. Proteins are highlighted that represent acidic patch binders and chromatin remodelers, and are colour coded according to the remodelling complex they belong to. FDR values were calculated using the Benjamini-

Hochberg procedure, as described in Methods. D) Table showing known chromatin remodelling complexes that are enriched in the μ Map dataset between H2A (WT) and H2A (3xAla). Proteins are colour coded by enrichment. Blue = Log₂FC > 0.5, FDR < 0.05. Cyan = Meets FDR requirement, FDR < 0.05. Red = Not enriched. Black = Not in dataset. Data shows that nucleosome binding for most (80%) of all complex members is affected by the deletion of the H2A acidic patch. E) Venn diagram showing overlap in the loss of function proteins in the H2A (WT) vs H2A (E92K) and H2A (WT) vs H2A (3xAla) datasets. Approximately two thirds of the hits (Log₂FC > 0.5, FDR < 0.05) observed in the H2A (E92K) experiment are also hits in the H2A (3xAla) experiment. For blot source data, see Supplementary Fig. 1.



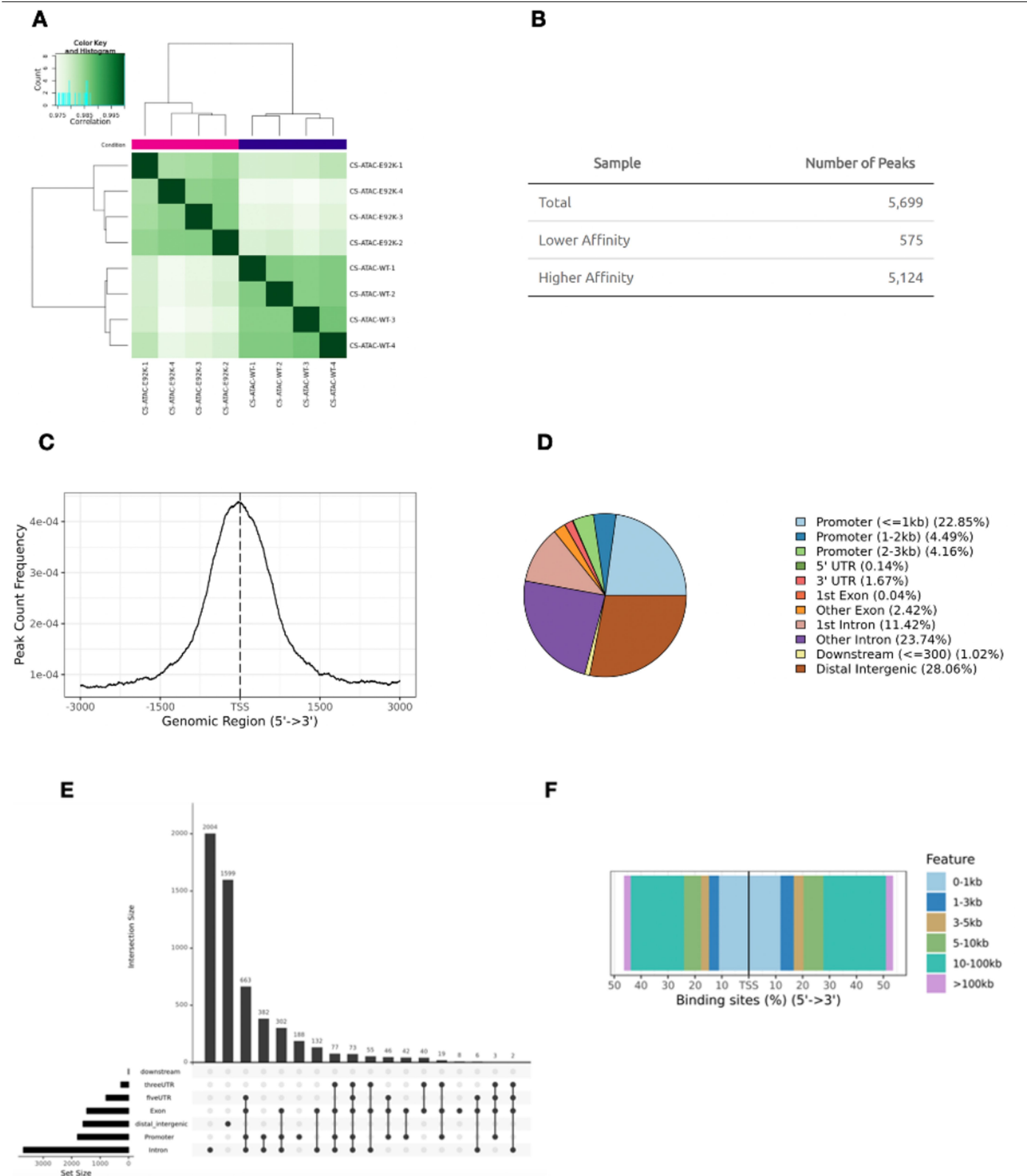
Extended Data Fig. 3 | Measurement of relative quantities of transfected histone H3.1. A) Representative western blot showing relative concentrations of native H3 and transfected H3.1-HA-Cfa^N-FLAG. B) Bar graph showing relative

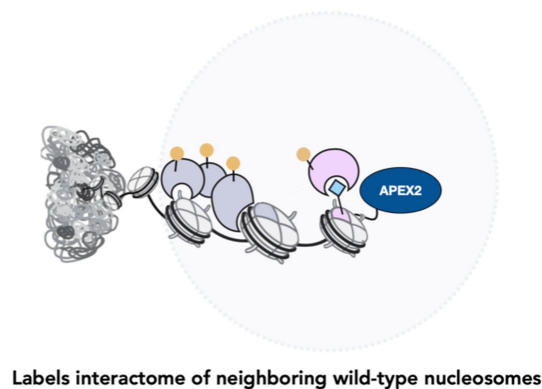
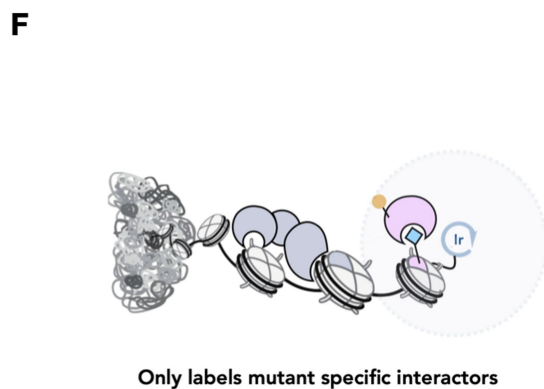
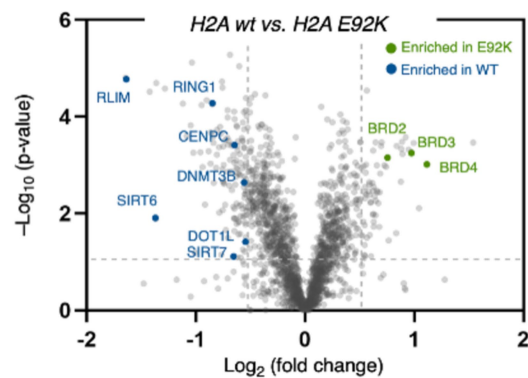
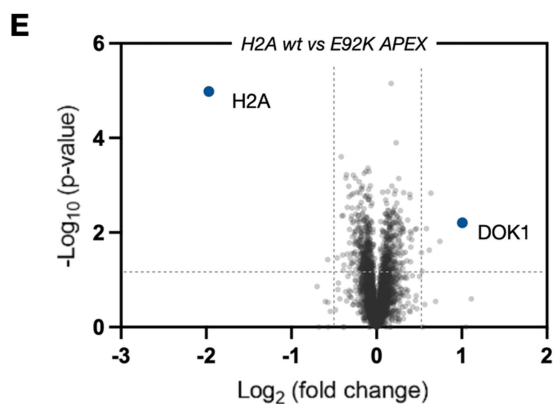
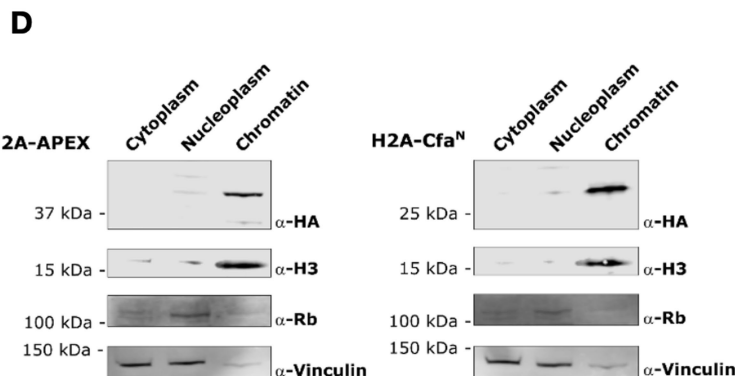
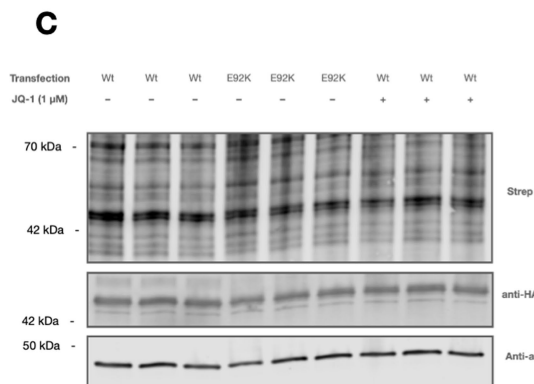
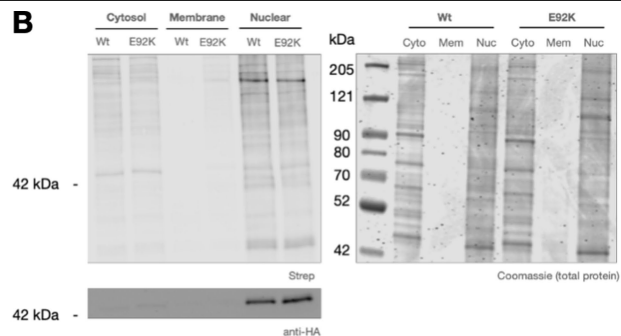
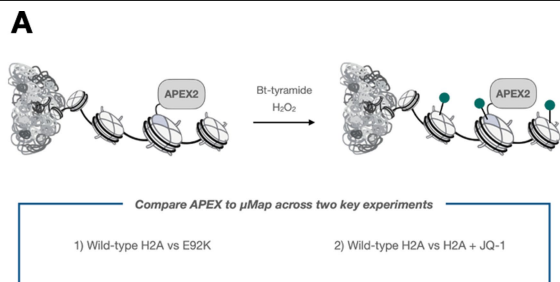
intensities of transfected and native H3. N = 6 independent biological replicates, (**** = $P < 0.0001$). Over 6 replicates transfected histones make up $\approx 1/12$ of all histone H3. For blot source data, see Supplementary Fig. 1.



Extended Data Fig. 4 | Comparison of proteomics data obtained from stable cell lines. To compare the effects of stable expression on μ Map we conducted our two core workflows in HEK 293T cells expressing H2A-HA-Cfa^N-FLAG and/or H2A(E92K)-HA-Cfa^N-FLAG. A) Anti-FLAG western blot showing stable expression of H2A-HA-Cfa^N-FLAG and H2A(E92K)-HA-Cfa^N-FLAG at the indicated viral titre. Ponceau staining is provided as a loading control. B) Left: Volcano plot derived from a two-sided t-test showing μ Map target ID experiment with JQ-1 in stably expressing cells with 1 μ M JQ-1. Data is consistent

with transiently transfected cell lines. Right: Volcano plot derived from a two-sided t-test showing μ Map experiment comparing wild-type and E92K interactomes. C) Comparison of H2A (WT) vs H2A (E92K) proteomics hits from transiently transfected cells compared to stably expressing cells. Table shows the four proteins investigated in this study. D) Venn diagram showing all proteins in common between datasets ($\text{Log}_2\text{FC} > 0.5$, $\text{FDR} < 0.05$). Overlap is observed for key chromatin modifying proteins. For blot source data, see Supplementary Fig. 1.

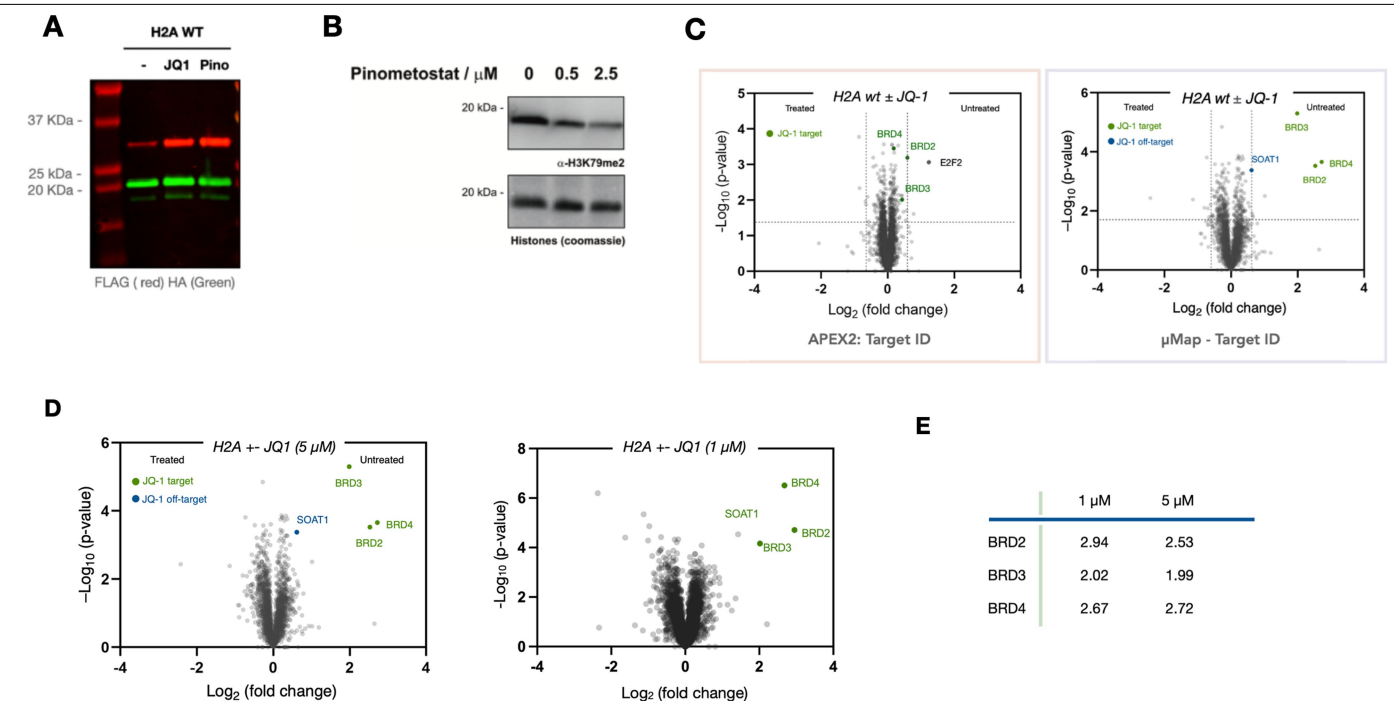




Extended Data Fig. 6 | See next page for caption.

Extended Data Fig. 6 | APEX2 comparison – Validation. Comparison of μ Map to APEX approaches: A) Key experiments in this study were repeated using previously reported APEX2 methodology according to the published procedure: Hung, V., Udeshi, N., Lam, S. et al. Spatially resolved proteomic mapping in living cells with the engineered peroxidase APEX2. *Nat Protoc* 11, 456–475 (2016). 10.1038/nprot.2016.018. B) Western blot showing relative levels of biotinylation in the fractionated nuclear, cytosolic and membrane proteome. Data shows that the APEX construct is localized to the nucleus. C) Western blot showing data from a 9-plex experiment representing two different experiments (H2A (WT) vs. H2A (E92K) and H2A \pm JQ-1; each N = 3). H2A-APEX2 expression and levels of biotinylation are even across all replicates. MW: H2A-HA-APEX2-FLAG = 41,981 Da. D) Fractionation of HEK 293T cells transfected with either H2A-APEX or H2A-Cfa^N shows that expressed HA-tagged histone fusion proteins are localized

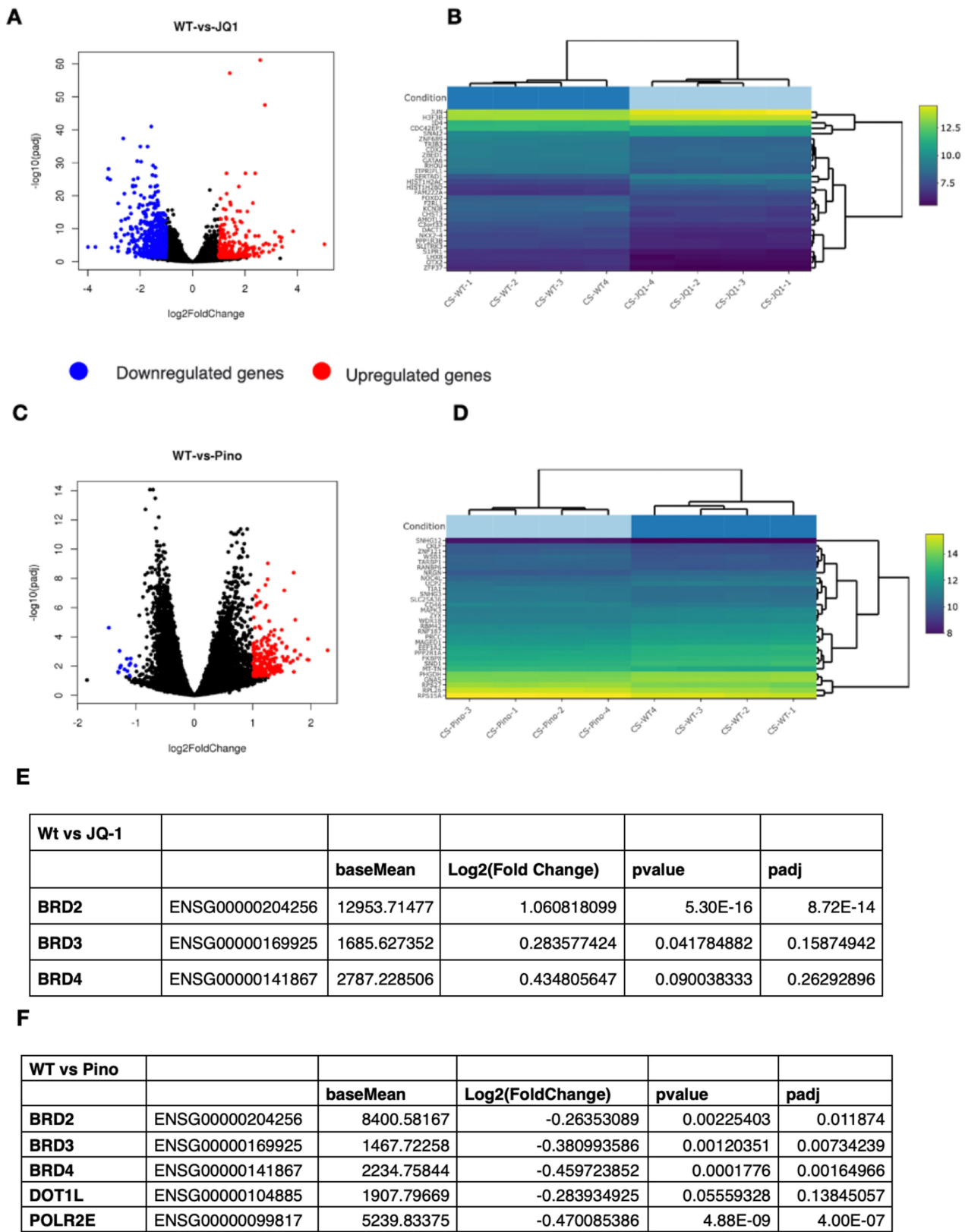
to the chromatin fraction. Left) Anti-HA western blot showing H2A-HA-APEX2-FLAG localization in different cellular fractions. Appropriate loading controls are provided. Right) Anti-HA western blot showing H2A-HA-Cfa^N-FLAG localization to different cellular fractions. Appropriate loading controls are provided. E) Volcano plots derived from a two-sided t-test showing comparison of results obtained from APEX2 proximity labelling and μ Map experiments for H2A (WT) vs H2A (E92K). F) Model for interactomes detected using APEX2 and Iridium conjugated nucleosomes. The short radius of μ Map only allows labelling of proteins directly interacting with the expressed nucleosome. The longer radius of APEX2 leads to additional labelling of the wild-type nucleosomal interactomes that border the expressed histone, leading to significant reduction in signal to noise. For blot source data, see Supplementary Fig. 1.



Extended Data Fig. 7 | Supporting data for H2A ± JQ-1 and Pinometostat.

A) *In nucleos* splicing reactions for H2A-Cfa^N constructs in the presence of Cfa^C-Ir as visualized by anti-HA/anti-FLAG western blot. Left (untreated cells), middle (cells treated with JQ-1), right (cells treated with Pinometostat). MW of H2A-HA-Cfa^N-FLAG = 28,121 Da. B) Treatment of HEK 293T cells with pinometostat for 24 h (0, 0.5, 2.5 μM) results in ≈60% decrease in H3K79 dimethylation, as visualized by western blotting with an anti-H3K79me2 antibody. Histones H3,

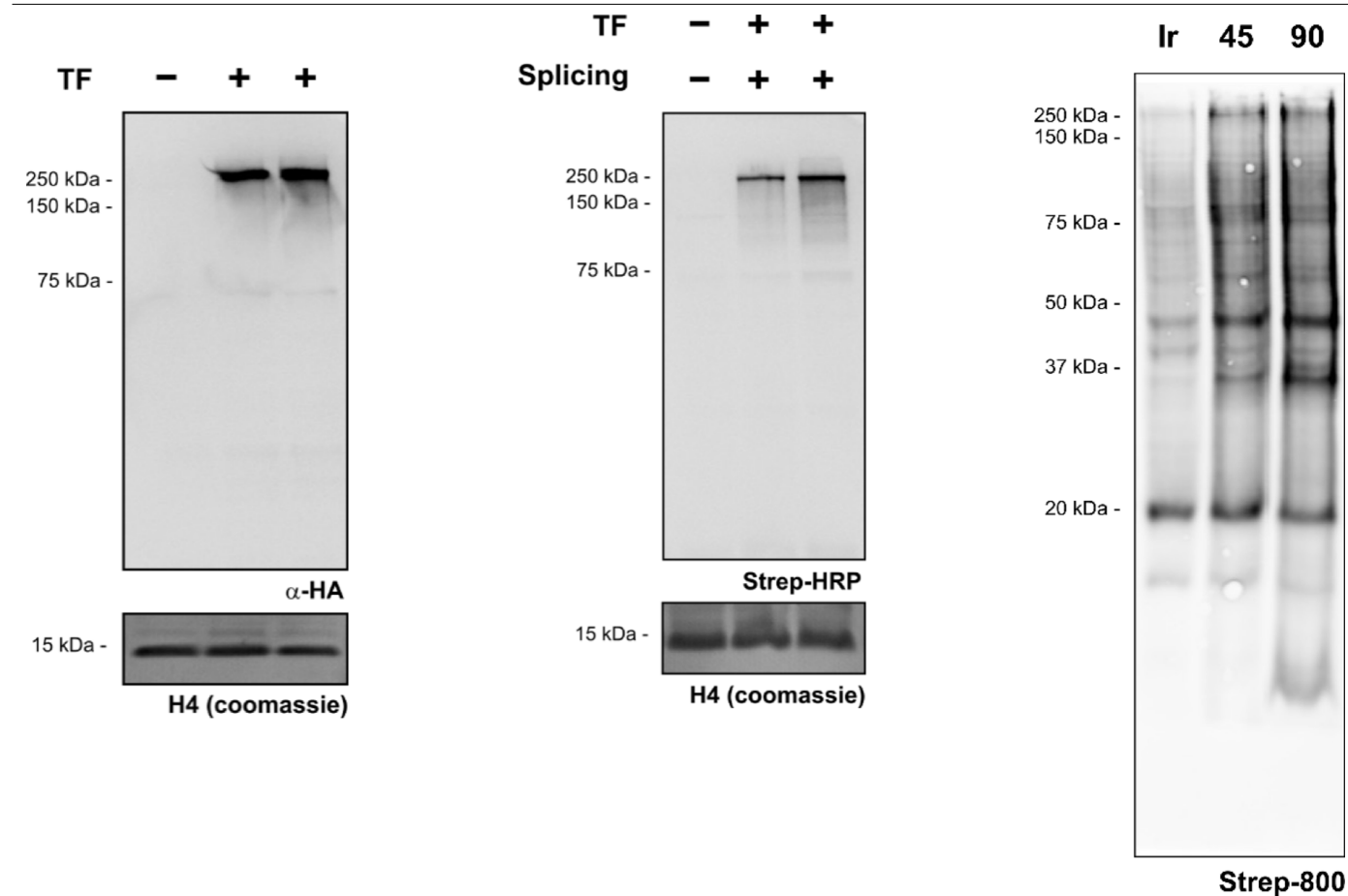
H2A, and H2B, stained by coomassie blue, are provided as a loading control. C) Volcano plots derived from a two-sided t-tests comparing APEX2 target ID proximity labelling to μMap target ID for H2A ± JQ-1. D) Volcano plot derived from a two-sided t-test for comparison of H2A ± JQ-1 at two different treatment concentrations (5 μM (left) and 1 μM (right)). E) Chart comparing the observed log₂ (fold change) values returned for BRD2/3/4 at the indicated treatment concentrations. For blot source data, see Supplementary Fig. 1.



Extended Data Fig. 8 | See next page for caption.

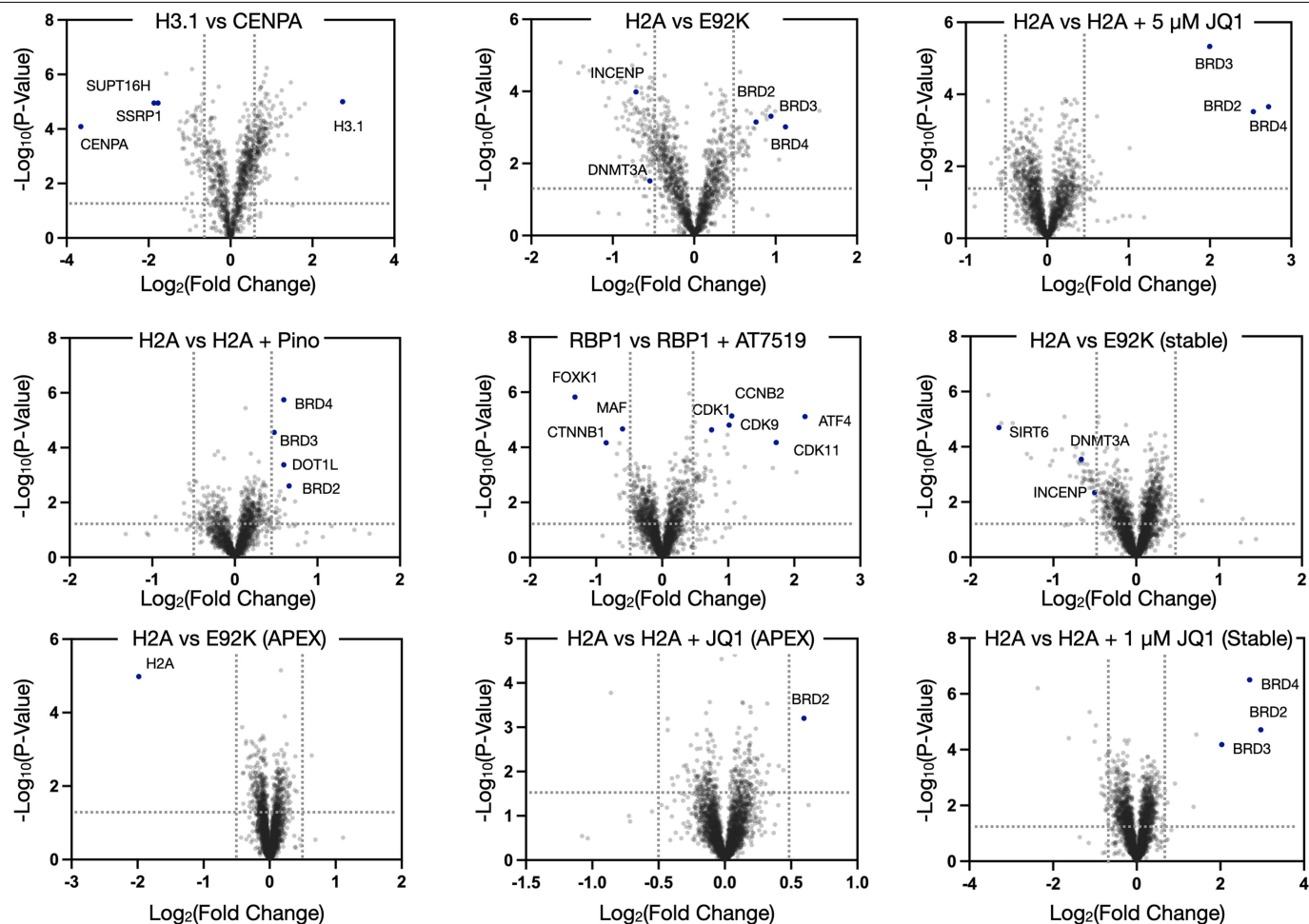
Extended Data Fig. 8 | RNA-Seq data. A) The global transcriptional change across the groups (WT vs JQ-1) compared was visualized by a volcano plot derived from a two-sided t-test. Each data point in the scatter plot represents a gene. The \log_2 fold change of each gene is represented on the x-axis and the \log_{10} of its adjusted p-value is on the y-axis. Genes with an adjusted p-value less than 0.05 and a \log_2 fold change greater than 1 are indicated by red dots. These represent up-regulated genes. Genes with an adjusted p-value less than 0.05 and a \log_2 fold change less than -1 are indicated by blue dots. These represent down-regulated genes. B) A bi-clustering heatmap was used to visualize the expression profile of the top 30 differentially expressed genes (WT vs JQ-1) sorted by their adjusted p-value by plotting their \log_2 transformed expression

values in samples. This analysis is useful to identify co-regulated genes across the treatment conditions. C&D) The same analysis was performed on (WT vs Pinometostat) samples. E) Table showing RNA-seq fold changes and P values for proteomic hits in from H2A vs H2A +JQ-1 experiment. Data strongly suggests that enrichment is due to proximity and not global changes in gene expression. F) Table showing RNA-seq fold changes and P values for proteomic hits in from H2A vs H2A + Pinometostat experiment. Data strongly suggests that enrichment is due to proximity and not global changes in gene expression. Importantly, genes enriched in proteomic analysis were NOT enriched in RNA-seq, showing enrichment is based on proximity, rather than changes in gene expression caused by ligand treatment.



Extended Data Fig. 9 | Validation of RBP1 expression and splicing. Left: Anti-HA western blot for the expression of RBP1-HA-Cfa^N-FLAG. H4 visualized by coomassie blue stain is provided as a loading control. Middle: *In nucleio* splicing reactions for RBP1-HA-Cfa^N-FLAG in the presence of Cfa^C-biotin (+) as visualized by streptavidin-800. H4 visualized by coomassie blue stain is

provided as a loading control. Right: Labelling of nuclear proteins after installation of Ir photocatalyst (45 and 90 s irradiation with blue LEDs) versus free Ir control as visualized by streptavidin-800. MW of RBP1-HA-Cfa^N-FLAG = 231,290 Da. For blot source data, see Supplementary Fig. 1.



Extended Data Fig. 10 | Volcano plots of all proteomics experiments analysed with two unique peptide filter. Volcano plots derived from a two-sided t-tests for MS experiments. All proteins presented require two

unique peptides found across all replicates. Cut-offs are Log₂FC > 0.5 and FDR < 0.05. For blot source data, see Supplementary Fig. 1.

Reporting Summary

Nature Research wishes to improve the reproducibility of the work that we publish. This form provides structure for consistency and transparency in reporting. For further information on Nature Research policies, see [Authors & Referees](#) and the [Editorial Policy Checklist](#).

Statistics

For all statistical analyses, confirm that the following items are present in the figure legend, table legend, main text, or Methods section.

- | n/a | Confirmed |
|-------------------------------------|--|
| <input type="checkbox"/> | <input checked="" type="checkbox"/> The exact sample size (n) for each experimental group/condition, given as a discrete number and unit of measurement |
| <input type="checkbox"/> | <input checked="" type="checkbox"/> A statement on whether measurements were taken from distinct samples or whether the same sample was measured repeatedly |
| <input type="checkbox"/> | <input checked="" type="checkbox"/> The statistical test(s) used AND whether they are one- or two-sided
<i>Only common tests should be described solely by name; describe more complex techniques in the Methods section.</i> |
| <input type="checkbox"/> | <input checked="" type="checkbox"/> A description of all covariates tested |
| <input type="checkbox"/> | <input checked="" type="checkbox"/> A description of any assumptions or corrections, such as tests of normality and adjustment for multiple comparisons |
| <input type="checkbox"/> | <input checked="" type="checkbox"/> A full description of the statistical parameters including central tendency (e.g. means) or other basic estimates (e.g. regression coefficient) AND variation (e.g. standard deviation) or associated estimates of uncertainty (e.g. confidence intervals) |
| <input type="checkbox"/> | <input checked="" type="checkbox"/> For null hypothesis testing, the test statistic (e.g. F , t , r) with confidence intervals, effect sizes, degrees of freedom and P value noted
<i>Give P values as exact values whenever suitable.</i> |
| <input checked="" type="checkbox"/> | <input type="checkbox"/> For Bayesian analysis, information on the choice of priors and Markov chain Monte Carlo settings |
| <input checked="" type="checkbox"/> | <input type="checkbox"/> For hierarchical and complex designs, identification of the appropriate level for tests and full reporting of outcomes |
| <input checked="" type="checkbox"/> | <input type="checkbox"/> Estimates of effect sizes (e.g. Cohen's d , Pearson's r), indicating how they were calculated |

Our web collection on [statistics for biologists](#) contains articles on many of the points above.

Software and code

Policy information about [availability of computer code](#)

Data collection	No software was used for data collection
Data analysis	Proteomic MS data was analysed using Maxquant (V2.1.3.0) (https://www.maxquant.org/) and Perseus (V2.0.6.0) (https://www.maxquant.org/perseus/) and plotted with Graphpad prism (V9) (https://www.graphpad.com/scientific-software/prism/). Heatmaps were plotted with Heatmapper (http://www.heatmapper.ca/). Venn Diagrams were generated using InteractiVenn (Heberle, H.; Meirelles, G. V.; da Silva, F. R.; Telles, G. P.; Minghim, R. InteractiVenn: a web-based tool for the analysis of sets through Venn diagrams. BMC Bioinformatics 16:169 (2015).)

For manuscripts utilizing custom algorithms or software that are central to the research but not yet described in published literature, software must be made available to editors/reviewers. We strongly encourage code deposition in a community repository (e.g. GitHub). See the Nature Research [guidelines for submitting code & software](#) for further information.

Data

Policy information about [availability of data](#)

All manuscripts must include a [data availability statement](#). This statement should provide the following information, where applicable:

- Accession codes, unique identifiers, or web links for publicly available datasets
- A list of figures that have associated raw data
- A description of any restrictions on data availability

The authors declare that all other data supporting the findings of this study are available within the paper and its supplementary information files. All relevant data are included in the manuscript and supplementary information. Mass spectrometry data files have been uploaded to the MassIVE proteomics database PXD038956/ <ftp://massive.ucsd.edu/MSV000090929/>. Sequencing data is available on the GEO database (GSE221674). FASTA files obtained from the UniProt Human Protein Database (<https://www.uniprot.org/>)

Field-specific reporting

Please select the one below that is the best fit for your research. If you are not sure, read the appropriate sections before making your selection.

☒ Life sciences ☐ Behavioural & social sciences ☐ Ecological, evolutionary & environmental sciences

For a reference copy of the document with all sections, see [nature.com/documents/nr-reporting-summary-flat.pdf](https://www.nature.com/documents/nr-reporting-summary-flat.pdf)

Life sciences study design

All studies must disclose on these points even when the disclosure is negative.

Sample size	Sample size (N>3) was chosen to ensure reproducibility and to obtain acceptable P-values
Data exclusions	No data was excluded
Replication	All experiments were performed with either three or four biological replicates
Randomization	Cellular samples were passaged to an appropriate volume and chosen at random for transfection or treatment.
Blinding	Blinding is not relevant to this study. All biological samples are processed in the same way and raw data is analyzed via computation.

Reporting for specific materials, systems and methods

We require information from authors about some types of materials, experimental systems and methods used in many studies. Here, indicate whether each material, system or method listed is relevant to your study. If you are not sure if a list item applies to your research, read the appropriate section before selecting a response.

Materials & experimental systems

n/a	Involved in the study
<input type="checkbox"/>	<input checked="" type="checkbox"/> Antibodies
<input type="checkbox"/>	<input checked="" type="checkbox"/> Eukaryotic cell lines
<input checked="" type="checkbox"/>	<input type="checkbox"/> Palaeontology
<input checked="" type="checkbox"/>	<input type="checkbox"/> Animals and other organisms
<input checked="" type="checkbox"/>	<input type="checkbox"/> Human research participants
<input checked="" type="checkbox"/>	<input type="checkbox"/> Clinical data

Methods

n/a	Involved in the study
<input checked="" type="checkbox"/>	<input type="checkbox"/> ChIP-seq
<input checked="" type="checkbox"/>	<input type="checkbox"/> Flow cytometry
<input checked="" type="checkbox"/>	<input type="checkbox"/> MRI-based neuroimaging

Antibodies

Antibodies used

Anti-FLAG Sigma Aldrich (M2) 1:1,000 in TBS-T
 Anti-HA Abcam (ab9110) 1:1,000 in TBS-T
 Anti-pan-Acetyl Abcam (ab21623) 1:1,000 in TBS-T
 Anti-H3 Abcam (ab1791) 1:5,000 in TBS-T
 Anti-H4 Abcam (ab31830) 1:1,000 in TBS-T
 Anti-H3K79me2 Abcam (ab3594) 1:1,000 in TBS-T
 Anti-SMARCA4 Santa Cruz (SC17796) 1:500 in TBS-T
 Anti-Rb Cell Signaling (CST9309) 1:1000 in TBS-T
 Anti-Vinculin Sigma Aldrich (9131) 1:1000 in TBS-T
 Anti-INCENP Cell Signaling (A841) 1:500 in TBS-T
 Anti-DNMT3a Invitrogen (PA1-882) 1:500 in TBS-T
 Anti-SIRT6 Invitrogen (PA5-17215) 1:500 in TBS-T
 Anti-Mouse LI-COR IRDye 680 nm 1:10,000 in TBS-T
 Anti-Rabbit LI-COR IRDye 800 nm 1:10,000 in TBS-T
 Streptavidin LI-COR IRDye Strep-800 nm 1:10,000 in TBS-T
 Anti-Mouse HRP conjugate Invitrogen (31430) 1:6,000 in TBS-T
 Anti-Rabbit HRP conjugate Bio-Rad (1706515) 1:3,000 in TBS-T

Validation

Anti-FLAG (Sensitivity Test: Detects 2 ng of FLAG-BAP fusion protein by dot blot using chemiluminescent detection. Specificity: Detects a single band of protein on a western blot from an E. coli crude cell lysate.)
 Anti-Ha (Positive control WB: 293FT cells transfected with 15kDa HA tagged Vpr (an HIV1 accessory protein))
 Anti-pan-Acetyl (Recognises proteins acetylated on lysine residues. Tested: acetylated histone, acetylated BSA, and acetylated MBP, no reaction to the non acetylated proteins.)
 Anti-H3 (1/1000 - 1/5000. Detects a band of approximately 17 kDa(predicted molecular weight: 15 kDa).Can be blocked with Human Histone H3 peptide (ab12149))

Anti-H4 (This antibody gave a positive signal in the following lysates: Calf Thymus Histone Preparation Nuclear Lysate HeLa Histone Preparation Nuclear Lysate Histone H4 Recombinant Protein)
 Anti-H3K79me2 (ab3594 detects a 17 kDa band in single lane Western Blot. Peptide inhibition in Western Blot hasn't been processed. Modification specificity is determined by Peptide Array. ab3594 binds strongly to the Histone H3 di methyl K79. In Peptide Array ab3594 also partially binds to mono methyl K79 and tri methyl K79 peptides.)
 Anti-SMARCA4 (Molecular Weight of Brg-1: 200-205 kDa. Positive Controls: HeLa nuclear extract: sc-2120.)
 Anti Rb: (Rb (4H1) Mouse mAb detects endogenous levels of total Rb protein. The antibody does not cross-react with the Rb homologues p107 or p130, or with other proteins.
 Anti-Vinculin (Monoclonal Anti-Vinculin specifically stains vinculin at cell-cell and cell-substrate contacts in tissue and cultured cells using indirect immunofluorescent labeling. The antibody reacts with the 116 kDa vinculin band in immunoblotting. The product reacts with vinculin of many species. Good reactivity is obtained with human, bovine, chicken, dog, rat, mouse, turkey, and Xenopus. The antibody shows cross reactivity with smooth muscle metavinculin.
 Specifically labels vinculin at cell-cell and cell-substrate contacts. Reacts strongly with human vinculin. Shows cross-reactivity with smooth muscle metavinculin.)
 Anti-INCENP (INCENP (A841) Antibody detects endogenous levels of total INCENP protein.)
 AntiDNMT3a (This Antibody was verified by Cell treatment to ensure that the antibody binds to the antigen stated. In utero SHS dysregulates the protein expression of DNMT3A, SERPINA1A, MAPK7, and PHF1 in male and female mice. a) Western blots show that DNMT3A and SERPINA1A were down-regulated, whereas MAPK7 and PHF1 were up-regulated in BALB/c male mice exposed in utero to SHS versus air-treated controls. b) Western blots show that SERPINA1A was down-regulated, whereas DNMT3A and MAPK7 were up-regulated in BALB/c female mice exposed in utero to SHS versus air-treated controls. c) Mean densitometry +/- SEM results showing fold change of treated mice versus controls for the proteins analyzed)
 Anti SIRT6 (this Antibody was verified by Knockdown to ensure that the antibody binds to the antigen stated. Antibody specificity was demonstrated by siRNA mediated knockdown of target protein. A549 cells were transfected with SIRT6 siRNA and reduction of signal was observed in Western Blot using SIRT6 Polyclonal Antibody (Product # PA5-17215))

Eukaryotic cell lines

Policy information about [cell lines](#)

Cell line source(s)	HEK293T (ATCC #CRL-321)
Authentication	None of the cell lines were independently authenticated
Mycoplasma contamination	None of the cell lines used were tested for mycoplasma contamination
Commonly misidentified lines (See ICLAC register)	No commonly misidentified cell lines were using in this study